Targeting tumour-intrinsic neural vulnerabilities of glioblastoma

Sohyon Lee[1]*, Tobias Weiss[2]*, Marcel Bühler[2], Julien Mena[1], Zuzanna Lottenbach[1], Rebekka Wegmann[1], Michel Bihl[3], Bartłomiej Augustynek[4], Sven Baumann[4], Sandra Goetze[5-7], Audrey van Drogen[5-7], Flavio Vasella[8], Elisabeth J. Rushing[9], Bernd Wollscheid[5-7], Matthias A. Hediger[4], Michael Weller[2], Berend Snijder[1,✉]

[1] Institute of Molecular Systems Biology, Department of Biology, ETH Zurich, Zurich, Switzerland.
[2] Department of Neurology, Clinical Neuroscience Center, University Hospital Zurich and University of Zurich, Zurich, Switzerland.
[3] Institute of Pathology, University Hospital Zurich, Zurich, Switzerland
[4] Membrane Transport Discovery Lab, Department of Nephrology and Hypertension and Department of Biomedical Research, Inselspital, University of Bern, Bern, Switzerland.
[5] Institute of Translational Medicine (ITM), Department of Health Sciences and Technology, ETH Zurich, Zurich, Switzerland.
[6] Swiss Institute of Bioinformatics, Lausanne, Switzerland.
[7] ETH PHRT Swiss Multi-Omics Center (SMOC), Switzerland.
[8] Department of Neurosurgery, Clinical Neuroscience Center, University Hospital and University of Zurich, Zurich, Switzerland
[9] Department of Neuropathology, University Hospital Zurich and University of Zurich, Zurich, Switzerland.
* Shared-first authorship.
✉ Correspondence to bsnijder@ethz.ch

Abstract

Glioblastoma is the most common yet deadliest primary brain cancer[1]. The neural behavior of glioblastoma, including the formation of synaptic circuitry and tumor microtubes, is increasingly understood to be pivotal for disease manifestation[2–8]. Nonetheless, the few approved treatments for glioblastoma target its oncological nature, while its neural vulnerabilities remain incompletely mapped and clinically unexploited. Here, we systematically survey the neural molecular dependencies and cellular heterogeneity across glioblastoma patients and diverse model systems. In 27 patient tumour samples taken directly after surgery, we identify a spectrum of cancer cell morphologies indicative of poor prognosis and discover a set of repurposable neuroactive drugs with consistent anti-glioblastoma efficacy. Glioblastoma cells exhibit functional dependencies on highly expressed neuroactive drug targets, while interpretable molecular machine learning (COSTAR) reveals their downstream convergence on AP-1-driven tumour suppression. This drug-target connectivity signature is confirmed by highly accurate *in silico* drug screening on >1 million compounds using COSTAR, as well as by multi-omic profiling of drug-treated glioblastoma cells. Thus, Ca^{2+}-driven AP-1 pathway induction represents a tumour-intrinsic vulnerability at the intersection of oncogenesis and neural activity-dependent signaling. Opportunities for clinical translation of this neural vulnerability are epitomized by the antidepressant Vortioxetine synergizing with current standard of care treatments *in vivo*. Together, the results presented here provide a mechanistic foundation and conceptual framework for the treatment of glioblastoma based on its neural origins.

Introduction

Glioblastoma is a deadly brain cancer with limited treatment options, shaped by heterogeneous developmental programs, genetic drivers, and tumor microenvironments [9–13]. Despite an increasing understanding of this heterogeneity, the alkylating agent Temozolomide (TMZ), which prolongs median survival from 12 to 15 months, remains the only first-line drug approved for glioblastoma [14–16]. Targeted therapies have been largely unsuccessful, in part due to the blood-brain barrier (BBB) limiting tumor accessibility, the presence of treatment-resistant glioblastoma stem cells (GSCs), and the lack of clinically predictive models [17–22]. Systemically addressing these therapeutic roadblocks is an urgent clinical need.

An emerging paradigm is to consider glioblastoma in the context of the nervous system. Single-cell RNA sequencing (scRNA-Seq) and lineage tracing studies of glioblastoma have identified stemness signatures resembling neural development [7,11,12,23–28]. At the brain-tumor interface, synaptic integration of cancer cells into neural circuits regulates tumor growth [5,6]. Within the tumor, the extension of microtubes akin to neuronal protrusions promotes the formation of treatment-resistant invasive networks [2,4,8]. Furthermore, modulating specific neurotransmitter or other secretory pathways in the tumor microenvironment impairs glioblastoma metabolism and survival [3,29–31]. Such neural aspects of glioblastoma offer new clinically-targetable vulnerabilities that could be exploited by repurposing approved “neuroactive” drugs (NADs). Neuroactive drugs can cross the BBB and are routinely prescribed for indications such as psychiatric or neurodegenerative diseases. Yet, as neuroactive drugs are originally developed to modulate the nervous system, their anti-cancer activity in glioblastoma patients is largely unknown.

Several key questions arise. First, how does neural intratumor heterogeneity across glioblastoma patients relate to disease course and response to therapy? Second, are there tumor-intrinsic neural vulnerabilities that are therapeutically targetable? Third, if so, which molecular dependencies and associated pathways are involved?

Here, we find morphological and neural stemness features across glioblastomas that relate to disease prognosis and drug response. Using pharmacoscopy (PCY), an *ex vivo* imaging platform [32–34] that captures patient and tumor complexity, we screen repurposable neuroactive drugs and identify a set with potent anti-glioblastoma activity. Top neuroactive drugs work consistently across patients and particularly target GSCs with neural morphologies associated with invasion and poor prognosis. These top drugs are validated across multiple glioblastoma model systems including patient-derived cultures and orthotopic xenograft mouse models. Integration of anti-glioblastoma response with multiplexed RNA-Seq, reverse genetic screening, and machine learning of drug-target networks reveals convergence of neuroactive drugs with anti-glioblastoma activity on AP-1 transcription factor and BTG tumor suppressor gene families. Using this drug-target connectivity signature, we predict and validate new candidate drugs across >1 million compounds *in silico*. The antidepressant Vortioxetine is the top PCY-hit and inducer of the AP-1/BTG signature, synergizing with both first- and second-line glioblastoma therapies *in vivo*. Our study identifies clinically-actionable neuroactive drugs for the treatment of glioblastoma converging on a gene regulatory network involved in cell proliferation and neural activity.

Results

Glioblastoma stem cell morphologies prognostic of poor outcome

Glioblastoma cells adopt unique cellular morphologies and stemness properties to integrate and survive in the brain [2,4,8,12,35]. To comprehensively profile morphological and molecular heterogeneity within and between glioblastoma patients, we performed high-content confocal imaging of freshly dissociated surgical samples across 27 patients (prospective cohort; Fig. 1a,b and Extended Data Fig. 1a). In parallel, for all patients, somatic genetic alterations were determined by targeted next-generation sequencing (NGS) and scRNA-Seq was performed for a subset of patients (n=4 patients, Fig. 1a, Extended Data Fig. 1a-f and Supplementary Table 1,2). Glioblastoma cells were identified and placed along a neural stemness gradient by scRNA-Seq and immunofluorescence against the neural progenitor marker Nestin and the mature astrocytic marker S100B (Fig. 1c,d and Extended Data Fig. 1c-e). Immune cells present in the tumor microenvironment (TME) were identified by the pan-immune marker CD45 and T cell marker CD3. Marker negative cells included additional TME cell types observed by scRNA-Seq or tumor cells with low protein levels of Nestin and S100B (Fig. 1c,d and Extended Data Fig. 1e,f). Patient samples were highly heterogeneous in composition, with Nestin+ or S100B+ glioblastoma cells ranging from 4-39%, CD45+ immune cells from 1-82%, and all marker negative cells 13-84% (Fig. 1d).

Nestin+ cells are a proliferative GSC subpopulation at the apex of the neural stemness gradient shown to sustain long-term tumor growth [17,19,36–38]. Upon visual inspection of Nestin+ GSCs, we observed cellular "morphotypes" distinguishable by the presence of tumor microtubes (TMs) and other morphological features such as cell size and shape (Fig. 1b,e-g). Using deep learning on 51,028 manually curated single-cell image crops across all patient samples, we trained a convolutional neural network (CNN) to classify Nestin+ cells into four main morphotypes (M1-M4) with 84.3% accuracy (Fig. 1d,f and Extended Data Fig.2a,b). Single-cell feature maps extracted from the CNN and nuclei segmentation revealed a continuum of M1-M3 morphotypes and a distinct cluster of small M4 cells (Fig. 1f,g). M1 (PTM; polygonal TM-containing) and M2 (ETM; elongated TM-containing) GSC morphotypes had varying distributions of TMs per cell (Fig. 1e), while TM-absent M3 (RB; round big) and M4 (RS; round small) morphotypes were characterized by their roundness yet differed in cell size (Fig. 1f,g and Extended Data Fig. 2c). Nestin expression was higher in the more complex M1-M3 morphotypes (Fig. 1g).

GSC morphotype composition varied dramatically across patients (M1: 1.3-31.4%; M2: 0.5-43.4%; M3: 1.9-38.6%; M4: 14-95.1%, Fig. 1d). Abundance of morphotypes was associated with cell proliferation, where the fraction of complex morphologies (M1-M3) was correlated with Ki67 levels measured by pathology in patient-matched tissue sections (Fig. 1h, top left). Furthermore, patient stratification based on morphotype composition was significantly associated with progression-free survival (PFS): lower baseline abundance of complex morphologies (M1, M3) and higher abundance of the small M4 morphotype was associated with better clinical outcome (n=17 patients with annotated PFS, Fig. 1h and Extended Data Fig. 2d). We did not observe a survival difference based solely on Ki67 levels, sex, or the abundance of marker-defined populations (Extended Data Fig. 2e); implying a unique prognostic contribution of the aggressive GSC morphologies. While *MGMT* promoter methylation status, a prognostic factor associated with response to alkylating agents, stratified patient survival, complex morphotype (M1-M3) abundance was independent of *MGMT* status (Fisher's test, P=0.19, Extended

Data Fig. 2e). Thus, while tumor microtubes have been associated with glioblastoma grade [2], we now show that GSCs adopt a spectrum of complex morphologies prognostic of poor clinical response also among glioblastomas.

Clinical concordance of *ex vivo* single-cell drug profiling

The DNA-alkylating chemotherapy TMZ remains the only approved first-line drug for glioblastoma. To determine if the chemosensitivity of highly heterogeneous patient samples relates to clinical response, we tested first- and second-line glioblastoma chemotherapies (n=3 drugs) in two independent glioblastoma cohorts: our main prospective cohort (n=27 patients) and a bio-banked retrospective cohort (n=18 patients, Fig.1a,i-l, Extended Data Fig. 3a, and Supplementary Table 1). We utilized pharmacoscopy (PCY), a clinically predictive *ex vivo* image-based screening platform developed in-house [32–34,39–42]. Pharmacoscopy measures the drug-induced relative reduction of any marker- or morphology-defined cell population in heterogeneous patient samples. Here, a positive PCY score indicates a reduction of Nestin+ or S100B+ glioblastoma cells relative to non-malignant TME cells, while a negative score indicates higher toxicity in the TME (Fig. 1i). Glioblastoma patients exhibited a wide spectrum of *ex vivo* responses to the first-line therapy Temozolomide (50-500µM; 2 days of incubation; Fig. 1j). We performed survival analysis on 16 of the 27 prospectively tested patients, limited to those patients with primary tumors and having received first-line TMZ treatment with evaluable PFS (n=16 patients, with n=3 ongoing responses). Prospectively stratifying patients by their *ex vivo* TMZ sensitivity suggested improved PFS for *ex vivo* responders, reaching significance at 100µM TMZ (p = 0.041; Fig. 1k and Extended Data Fig. 3b). We repeated this PCY-based response stratification analysis in a retrospective validation cohort with documented PFS and OS (n=18 patients). Here, *ex vivo* TMZ responders also had significantly longer PFS and OS, evidenced across all four tested TMZ concentrations (Fig. 1l). In contrast, TMZ sensitivity of CD45+ immune cells or of GSC morphotypes was not associated with clinical response. *Ex vivo* TMZ response further related to *MGMT* status, as we observed higher sensitivities to low dose TMZ (50µM) in patient tumors with methylated *MGMT* promoter (Extended Data Fig. 3c). Taken together, this suggests that *ex vivo* TMZ response of glioblastoma cells, as well as the baseline abundance of GSC morphotypes at diagnosis, are both novel prognostic factors for first-line response. The concurrence of pharmacoscopy with clinical response establishes the utility of image-based drug screening in patient material for the discovery of new glioblastoma therapies.

Therapeutically targeting neural tumor heterogeneity

The question arises whether it is possible to pharmacologically target the heterogeneous spectrum of malignant cells, both in terms of their molecular composition and morphological nature. To find repurposable drug candidates that target glioblastoma cells and aggressive GSC morphologies, we tested both neuroactive and oncology drug libraries across the prospective glioblastoma cohort (Fig. 2a-c, Extended Data Fig. 3d,e, and Supplementary Table 3). The neuroactive drug (NAD) library consisted of drugs approved for neurological diseases such as depression, epilepsy, and Alzheimer's disease (n=67 drugs; 20µM). The oncology drug (ONCD) library included therapies approved for solid tumor indications such as cyclin-dependent kinase (CDK) and receptor tyrosine kinase (RTK) inhibitors (n=65 drugs; 1 and 10µM). We screened the NAD library across the whole prospective cohort (n=27 patients) and additionally tested the ONCD library in a subset of patients when enough surgical material was available (n=12 patients). As primary PCY-readouts, we measured on-target reduction of

Nestin+ or S100B+ cells and GSC morphotype composition changes across patients (Fig. 2b,c and Extended Data Fig. 3d). Drug responses for other TME populations including immune cells and marker negative cells were also measured (Extended Data Fig. 3e).

Despite limited success of targeted cancer therapies for glioblastoma, opportunities for molecularly-guided precision oncology and drug repurposing remain. Among ONCDs, the top mean ranking PCY-hit across patients was Elesclomol, a BBB-penetrant mitochondrial oxidative stress-inducer (Fig. 2c and Extended Data Fig. 3d) [43,44]. Elesclomol represents a compelling therapeutic candidate amidst growing evidence highlighting the importance of mitochondrial dynamics in brain tumorigenesis [45–47]. Among all tested drugs, Elesclomol response showed the strongest positive correlation with age, suggesting a potential link with mitochondrial aging and benefit for elderly patients (Fig. 2d). Ranked 2nd and 6th among the ONCDs were the two structurally-related multi-tyrosine kinase inhibitors, Sorafenib and Regorafenib. Regorafenib has recently been proposed to mediate a survival benefit over Lomustine in a randomized phase II clinical trial for patients with recurrent glioblastoma (Fig. 2c and Extended Data Fig. 3d) [48]. Across our cohort, Regorafenib showed one of the strongest positive correlations to Ki67 levels, which could be leveraged to inform future clinical trials (Fig. 2e). Conversely, both of the tested mTOR inhibitors Temsirolimus and Everolimus showed no *ex vivo* efficacy, in line with negative results from randomized clinical trials (Extended Data Fig. 3d) [49–51]. As a tumor's mutational profile often influences drug response, we examined associations between ONCD responses and genetic alterations measured by targeted NGS across the cohort. The strongest pharmacogenetic association for ONCDs was the markedly increased *ex vivo* sensitivity of patients carrying p53 mutations to the CDK4/6 inhibitor Abemaciclib (Fig. 2f and Extended Data Fig. 3f-g). Our exploratory analysis of oncological drugs approved for other indications thereby identifies unevaluated treatment opportunities in glioblastoma.

Neuroactive drugs, in contrast, are developed to cross the blood-brain barrier and act upon the nervous system. Among NADs, we identified 15 of 67 drugs (22%) with consistent anti-glioblastoma activity across patients (top NADs; PCY-hits; mean PCY score > 0.03). Top NADs effectively reduced fractions of aggressive GSC morphologies in patient samples (M1-M3), and showed activity across patient-derived cultures (PDCs, n=3 lines) and established glioblastoma cell lines (n=4 lines, Fig. 2a,b). Dose-response relationships were further confirmed in glioblastoma cell lines for selected top NADs (n=9 drugs, Extended Data Fig. 4a-d). The top mean ranking PCY-hit was Vortioxetine, a safe and novel class of antidepressant with previously unknown anti-glioblastoma activity (Fig. 2b,c). Strikingly, Vortioxetine was more potent in patient samples with higher baseline abundance of aggressive GSC morphologies (Fig. 2g). Vortioxetine was also the most consistently effective drug across all tested glioblastoma model systems, with *ex vivo* efficacy surpassing Regorafenib (Fig. 2c). Other clinically attractive NADs included Paroxetine and Fluoxetine, both antidepressants of the selective serotonin reuptake inhibitor (SSRI) class, and Brexpiprazole, an atypical antipsychotic used for the treatment of schizophrenia. Brexpiprazole *ex vivo* response was related to sex, where men responded better than women (Fig. 2h and Extended Data Fig. 3g). Not all top NADs were clinically suitable considering the historically reported side-effects of the cannabinoid receptor blocker Rimonabant and the antipsychotic Zotepine, yet these could still inform future drug design studies.

Notable exceptions to the pan-patient and model consistency of top NADs were Apomorphine, Olanzapine, and Sertindole (Fig. 2b). Apomorphine showed high TME toxicity in a subset of patient samples and diminished efficacy in PDCs and glioblastoma-initiating spheroid cell lines (ZH-161, ZH-562); Olanzapine showed diminished activity against aggressive GSC morphologies, PDCs, and cell lines;

and Sertindole response was highly variable among patients, despite its potency in glioblastoma models. Patient variability in *ex vivo* Sertindole response was related to the loss of FGFR2 (copy number variation; CNV loss), representing the most significant pharmacogenetic NAD association (Fig. 2i and Extended Data Fig. 3f).

Here, by comprehensively screening across heterogeneous patients and model systems, we identify a set of repurposable neuroactive drugs that effectively target the neural heterogeneity of glioblastoma cells. The consistency of the anti-glioblastoma efficacy of these neuroactive drugs in diverse model systems even in the absence of the TME suggests that they are targeting tumor-intrinsic vulnerabilities.

Divergent functional dependencies on neuroactive drug targets

The multitude of neuroactive drugs with anti-glioblastoma activity was unexpected, prompting the question as to whether there could be shared underlying mechanisms. Top NADs represented diverse drug classes without significant enrichment, indicating that canonical mode-of-action did not explain drug efficacy (Fig. 3a). This is in line with a previous screen of neurochemical compounds in patient-derived stem cell lines, which found various neurochemical classes represented among their hits [29]. Among our tested serotonin and dopamine pathway modulators, for example, only 4 out of 11 antidepressants (36%) and 6 out of 16 antipsychotics (38%) exhibited anti-glioblastoma activity in primary patient samples on average (Extended Data Fig. 4e). Such drug classifications, however, simplify the polypharmacological drug-target profiles of neuroactive drugs. The majority of NADs act on multiple primary target genes (PTGs). These include ion channels, GPCRs, and enzymes that modulate neurotransmission in the central nervous system, whose expression remains a largely unexplored dimension of glioblastoma heterogeneity. Dependency on neuroactive PTGs with high lineage specificity and consistent expression across patients could explain the activity of top NADs.

We first set out to determine the expression of NAD PTGs by scRNA-Seq. We integrated scRNA-Seq data from our glioblastoma patient cohort (n=4 patients) with two published data sets (*Neftel et al.*,n=9 patients; *Yu et al.*, n=9 patients, Fig. 3b,c and Extended Data Fig. 5a,b) [12,28]. Collectively, we profiled 22 glioblastoma patient single-cell transcriptomes across 25,510 cells for their expression of PTGs with biochemical NAD-interactions reported in the Drug Targets Commons database (DTC) [52]. Among these PTGs, certain classes of ion channels and GPCRs were enriched in neural lineage cells (e.g. potassium, glutamate, and cannabinoid), while other classes showed broader expression patterns (e.g. calcium, adrenaline, Extended Data Fig. 5a). To quantify PTG expression across cell types and patients, we defined neural- and patient-specificity scores (NS and PS; Fig. 3b, Extended Data Fig. 5b and Methods). For detected genes, a higher NS indicates relative enrichment in glioblastoma cells (range -1 to 1) and a higher PS (range 0 to 1) indicates more patient-specific expression, while both scores will be close to zero for low-abundance genes. We first benchmarked the neural- and patient-specificity scores against the whole transcriptome for each dataset, including key glioblastoma (Nestin, S100B, CD133, SOX2) and immune marker genes (CD45, CD3, CD14) that were on expected opposites of the NS spectrum (Extended Data Fig. 5b and Supplementary Table 4). Among PTGs, ion channels and receptors with high neural-specificity included the calcium signaling modulator SIGMAR1, glutamatergic AMPA receptor subunit GRIA2, and cannabinoid receptor CNR1 (Fig. 3c). Patient-specificity for neurological receptors SIGMAR1 and CNR1 were on average 1.7 to 3-fold lower than for oncogenic RTKs EGFR and PDGFRA, despite similar detection levels. Thus, we find abundant and consistent pan-patient expression of neuroactive drug targets on glioblastoma cells, confirmed across independent cohorts.

We next tested genetic dependencies on these NAD PTGs by performing an siRNA screen in LN-229 glioblastoma cells (n=59 genes, Fig. 3d and Extended Data Fig. 5c,d). LN-229 cells were confirmed to have patient-comparable PTG expression as well as neuroactive drug responses (Fig. 2b, Fig. 3d and Extended Data Fig. 5d). A significant decrease in cell viability was observed upon knockdown of 9 PTGs, including ADRA2B, SIGMAR1, DRD1, HTR3A, and MC3R (Fig. 3d and Extended Data Fig. 5c,d). Of these, ADRA2B and MC3R expression levels stratified glioblastoma patient survival in The Cancer Genome Atlas (TCGA) cohort (Extended Data Fig. 5e). However, these primary drug targets representing genetic dependencies were all annotated in DTC to predominantly interact with drugs that showed no activity by pharmacoscopy. Inversely, top neuroactive drugs had many annotated targets not representing genetic dependencies. For example, based on DTC, only 6 of the 17 NADs interacting with ADRA2B were PCY-hits, and only 1 out of 11 NADs interacting with HTR3A was a PCY-hit (Fig. 3e). Therefore, while presenting novel neural vulnerabilities, no PTG dependency uniquely explained the majority of our top neuroactive drugs.

Anti-glioblastoma activity explained by drug-target convergence

Despite their chemical and primary target diversity, our top NADs may still converge upon common downstream signaling pathways. To test this, we developed an interpretable machine learning approach called COSTAR: *convergence of secondary drug targets analyzed by regularized regression.* COSTAR is designed to identify the minimal drug-target connectivity signature predictive of efficacy.

We expanded the drug-target search space to include PTGs with any bioactivity annotated by DTC, termed extended PTGs (ePTGs). Secondary target genes (STGs) downstream of ePTGs were subsequently mapped by high-confidence protein-protein interactions annotated in the STRING database (Fig. 3f). This resulted in a drug-target connectivity map, or “COSTAR constellation”, of all DTC-annotated drugs in our NAD and ONCD libraries (n=127 of 132 tested drugs) with 975 extended primary targets, 10,573 secondary targets, and 114,517 network edges (Fig. 3f). Using logistic LASSO regression, we trained a multi-linear model that identifies the minimal set of STGs that maximally discriminates PCY-hit drugs (n=30; top-15 drugs from both NADs and ONCDs) from PCY-negative drugs (n=97; all other tested drugs) in a cross-validation setting (Fig. 3f,g Extended Data Fig. 6a, and Methods). Thereby, COSTAR converged upon the most simplistic connectivity signature that was predictive of anti-glioblastoma drug efficacy (Fig. 3h and Extended Data Fig. 6a,b). Encouragingly, COSTAR identified a signature that classified the 127 drugs in our training data with 92.1% accuracy, correctly predicting 20/30 PCY-hits and 96/97 negative drugs (Fig. 3g).

The COSTAR connectivity signature predominantly linked PCY-hit NADs to the secondary target BTG2 through JUN/TP53 ePTGs (Fig. 3h and Extended Data Fig. 6b). BTG2 and TP53 are both tumor suppressors that control cell cycle and differentiation, while JUN is a member of the AP-1 transcription factor (TF) family that regulates gene expression in response to stimuli such as neural activity [53,54]. Conversely, the majority of PCY-hit ONCDs were connected to the secondary target AP1S2, a protein involved in clathrin assembly, through the cyclin G-associated kinase GAK (Fig. 3h and Extended Data Fig. 6b). A subset of PCY-hit ONCDs were also linked to BTG2 through cyclins CCND1 and CCNH, while a subset of PCY-hit NADs were linked to AP1S2 through RAB9A, a member of the RAS oncogene family (Fig. 3h). Taken together, this reveals pathway convergence on AP-1 transcription factors and cell cycle regulation as a unique signature predictive of anti-glioblastoma activity of neuroactive drugs.

COSTAR can be utilized as a powerful *in silico* drug screening tool. It can match the drug-target profile of any annotated compound with the identified connectivity signature to predict its hit probability (COSTAR score). To experimentally validate the COSTAR signature and find additional neuroactive drug candidates with anti-glioblastoma activity, we computationally screened across 1,120,823 DTC-annotated compounds and selected 48 previously untested repurposable and BBB-permeable drugs among the top and bottom scoring compounds (COSTAR-hits and COSTAR-negs resp.; Fig. 3i-k). All predicted COSTAR-hits (n=23 drugs) were linked to the secondary target BTG2. Conversely, none of the COSTAR-negs (n=25 drugs) had annotated connections to BTG2 (Extended Data Fig. 6c). To validate these COSTAR predictions, we tested all 48 drugs across four GBM patient samples *ex vivo* (P030, P032, P034, P042), and observed excellent agreement between COSTAR predictions and experimental results (mean AUC=0.94, Fig. 3j,k). The new COSTAR-hits again represented diverse drug classes, including the antipsychotic Trifluoperazine, antiparkinsonian Ethopropazine, antidepressant Sertraline, and bronchodilator Salmeterol (Fig. 3j). These results validate our interpretable molecular machine learning approach for *in silico* drug discovery, and confirm AP-1 and cell cycle pathway convergence as a predictive signature of neuroactive drugs with *ex vivo* anti-glioblastoma activity.

From neural activity-dependent signaling to tumor suppression

Convergent drug targets of top NADs represent transcription factors and tumor suppressors, suggesting common gene regulatory networks (GRNs) underlying the anti-glioblastoma activity of NADs. To determine transcriptional changes upon drug perturbation, we profiled 20 drug responses across two time-points (6 and 22 hours) in LN-229 cells by DRUG-Seq [55,56]. These 20 drugs were selected to include PCY-hit NADs spanning diverse drug classes (n=11), PCY-hit ONCDs (n=7), PCY-negative NADs (n=2), and a DMSO control (Fig. 4a-d, Extended Data Fig. 7a,b, and Supplementary Table 3). Differential gene expression analysis upon PCY-hit NAD treatment compared to the PCY-negative NADs and DMSO control revealed a strong transcriptional drug response, with upregulated genes enriched in 'MAPK signaling' and 'transcriptional misregulation of cancer' pathways at both time-points (Fig. 4b and Extended Data Fig. 7c,d).

In remarkable alignment with COSTAR, AP-1 and BTG family member genes were strongly upregulated in response to the PCY-hit NADs (Fig. 4b,d and Extended Data Fig. 7e). This upregulation was observed even for Vortioxetine and Brexpiprazole, both lacking DTC-annotations at the time of analysis and thus not contributing to the COSTAR training (Fig. 4d). We saw rapid and sustained upregulation of AP-1 TFs JUN and FOS, as well as BTG1, a close homologue of BTG2 identified by COSTAR [57,58] (Fig. 4b,d). JUN and FOS are context-dependent oncogenic factors as well as canonical 'immediate-early genes' (IEGs) that are rapidly induced upon neural activity [53,54,59]. The presence of other upregulated IEGs, including NR4A1, EGR1 and ARC, strengthened this surprising involvement of neural-activity dependent signaling in glioblastoma (Fig. 4b).

To find key upstream regulators mediating the transcriptional response to PCY-hit NADs, we performed transcription factor binding-site (TFBS) enrichment analysis of the upregulated genes (Fig. 4c and Extended Data Fig. 7f). The most significantly enriched TF motifs at 6 hours were AP-1, ATF (a member of the AP-1 superfamily), and CREB (a calcium-activated regulator of AP-1 transcription) [53,60,61] (Fig. 4c). Not only were AP-1 TFs the most enriched binding domain, but their own expression was also directly induced upon PCY-hit NAD treatment (Fig. 4b,d and Extended Data Fig. 7e). ATF3 was the most significantly upregulated gene across both time-points, while ATF4, JUN, JUNB, FOS, and FOSB were among top differentially expressed genes (Fig. 4b,d and Extended Data Fig. 7c). Induction of AP-1

factors was primarily NAD-specific, where ONCD treatment did not elicit a similar global transcriptional response (Fig. 4d and Extended Data Fig. 7c). Though NAD-induced AP-1 expression was sustained across both time-points, TFBS enrichment analysis of upregulated genes at the 22 hour time-point identified forkhead TF family members (e.g. FOXO1, FOXO3, FOXD3, HFH1) as a gene regulatory module succeeding AP-1 Extended Data Fig. 7f). AP-1 and forkhead TFs have well-established roles in mediating immediate-early response to neural activity and regulating long-term cell differentiation, respectively [53,54,62–64].

Upstream of AP-1, a rapid Ca^{2+} influx and calcium-dependent signaling typically precede IEG expression and AP-1 activation [53,61,65,66]. We therefore measured both NAD-mediated endoplasmic reticulum (ER) calcium store release as well as extracellular calcium influx in LN-229 cells by high-throughput FLIPR calcium assays (n=17-18 drugs; Supplementary Table 3). While none of the tested drugs triggered ER Ca^{2+} store release, we observed an immediate and strong extracellular Ca^{2+} influx in response to 5 out of 8 of our PCY-hit NADs (Fig. 4e,f and Extended Data Fig. 8a,b). The strongest Ca^{2+} influx was observed upon Vortioxetine treatment, while two additional antidepressant hits, Paroxetine and Fluoxetine, also elicited strong responses (Fig. 4e,f). In contrast, the PCY-neg NADs (n=6) including two other antidepressants, and ONCD-hits (n=2; Elesclomol, TMZ) did not trigger calcium influx (Fig. 4e,f). These results demonstrate that, for the majority of our top NADs, a rapid drug-induced Ca^{2+} influx precedes IEG upregulation and subsequent anti-glioblastoma activity.

Downstream of AP-1, we evaluated whether BTG tumor suppressors could be direct effectors of the AP-1 gene regulatory network. BTG1 was one of the top 20 most significantly induced genes by the PCY-hit NADs (Fig. 4b,d and Extended Data Fig. 7c). BTG2 was strongly induced in specific conditions, including Vortioxetine and Paroxetine treatment (Fig. 4d). To delineate regulators of BTG family genes, we leveraged genome-wide mapping of transcriptional regulatory networks by PathwayNet, a tissue-aware data integration approach that utilizes 690 ChIP-Seq datasets from the ENCODE project [67]. The most enriched transcriptional regulators of BTG1/2 were members of the AP-1 TF network (e.g. JUN, ATF3, FOS), implying BTG tumor suppressor gene expression is directly mediated by AP-1 factors (Fig. 4g).

Congruence between NAD-induced AP-1 activation and its anti-glioblastoma activity would strengthen a causal role for this gene regulatory network. Remarkably, drug-induced expression of AP-1 TFs and BTG genes (the 'COSTAR signature') was highly correlated with a drug's *ex vivo* anti-glioblastoma efficacy in patient samples (R=0.72, *P*=1.4e-05; Fig. 4h). We additionally performed BTG1/2 and JUN loss-of-function experiments by siRNA-mediated knockdown in LN-229 cells. Quantitative RT-PCR after 72 hours of gene silencing confirmed reduced expression of BTG1/2 and JUN and revealed interdependent regulatory interactions governing their expression (Extended Data Fig. 8c). BTG1 but not BTG2 inhibition accelerated cell growth measured by live-cell imaging across 7 days (Fig. 4i). Increased cell proliferation upon BTG1 inhibition was also validated by endpoint pharmacoscopy after 3 days (Fig. 4j). By DRUG-Seq analysis, BTG1 induction represented a pan-NAD signature, while BTG2 was induced only in specific drug conditions such as Vortioxetine treatment (Fig. 4d). Vortioxetine also triggered the strongest calcium increase and represented the most effective NAD overall by pharmacoscopy. We therefore next evaluated the functional dependencies of Vortioxetine anti-glioblastoma efficacy on BTG1/2 and JUN. After two days of siRNA-mediated gene silencing and one subsequent day of drug treatment, BTG1 inhibition rescued Vortioxetine-mediated cell death (Fig. 4j).

Together, these results propose a model in which a subset of neuroactive drugs mediate anti-glioblastoma activity by triggering a rapid calcium influx, IEG and AP-1 transcription factor activation,

followed by engagement of an antiproliferative program that includes BTG-driven tumor suppression (Fig. 4k).

Potent and rapid AP-1 induction by Vortioxetine

To closer examine the temporal dynamics of the most effective neuroactive drug, Vortioxetine, we performed in-depth transcriptomic and proteomic profiling at 3-6 time-points in LN-229 cells (Fig. 5a and Extended Data Fig. 8d-h). Gene expression change over time was the strongest driver of variance in Vortioxetine-treated RNA samples analyzed by principal component analysis (Extended Data Fig. 8d). Among the top 100 gene loadings for PC1 (38.9% explained variance), we observed induction of AP-1 TFs FOS, JUNB, ATF4, and the AP-1 effector gene ARC already at 3 hours (Fig. 5a and Extended Data Fig. 8e). At the RNA level, 10 AP-1 TFs were significantly upregulated at all time-points, with temporal dynamics depending on individual TFs (Fig. 5a and Extended Data Fig. 8e). At the protein level, gene set enrichment analysis (GSEA) at 3 hours revealed DNA-binding transcription activator activity as the most over-represented gene ontology (GO) term (Extended Data Fig. 8f-h). Rapid and sustained protein expression of AP-1 TFs was observed between 3 and 9 hours, coinciding with upregulation of BTG1/2 and other negative regulators of cell cycle such as CDKN1B and PPM1B (Fig. 5a and Extended Data Fig. 8f,h). Significant activation of MAPK, ER stress response, and DNA damage pathways were also observed (Fig. 5a). Conversely, cytoskeletal components and oncogenic RTKs associated with the malignant phenotype of glioblastoma, including EGFR, NTRK2, and PDGFRA, were downregulated upon Vortioxetine treatment (Fig. 5a).

AP-1 activity and function in tumorigenesis can be context- and cell type-dependent [59]. Consequently, we set out to confirm AP-1 induction upon NAD treatment in compositionally heterogeneous glioblastoma patient samples taken directly after surgery. We examined AP-1 expression both at the single-cell gene and protein level.

We first performed scRNA-Seq on cells from patient P024 following 3 hours of *ex vivo* Vortioxetine treatment (Fig. 5b,c and Extended Data Fig. 9a,b). Analysis of 1736 single-cell transcriptomes revealed 4 main clusters with intermixed Vortioxetine-treated and DMSO-control cells (Extended Data Fig. 9a). Cluster 1 represented the most malignant cluster with highest expression levels of glioblastoma stemness markers such as Nestin, Ki67, CCND2, and VEGFA. Cluster 2 and 3 also expressed glioblastoma stemness markers, at lower levels than cluster 1. Cluster 4 represented an immune cluster, with the highest expression of the pan-immune marker CD45 (Fig. 5b and Extended Data Fig. 9b). Per-cluster comparison of Vortioxetine-treated versus DMSO-control cells revealed glioblastoma-specific induction of AP-1 factors upon Vortioxetine treatment (Fig. 5c). For example, JUNB, JUND, and AP-1 effector gene ARC were upregulated in cluster 1, while ATF4 and MAF were induced in all three glioblastoma clusters (cluster 1-3), with a more pronounced induction of ATF4 in clusters 2 and 3 (Fig. 5c).

Next, we performed immunofluorescence against JUND, ATF4, FOS and the AP-1 effector gene HOMER1 in three additional glioblastoma patient samples (P039, P040, P042) after Vortioxetine treatment (Fig. 5d,e). AP-1 factor induction in Nestin+ glioblastoma cells was observed in a patient-, time-point, and concentration-dependent manner. The strongest induction of all tested AP-1 factors was seen in patient sample P040 that had high abundance of complex morphotypes (M1-M3), which were reduced upon Vortioxetine treatment (Fig. 5d,e). HOMER1 and ATF4 were induced in all three patient samples, while FOS and JUND exhibited more patient variability (Fig. 5d). Together, this

detailed analysis of Vortioxetine response highlights the added layer of complexity relating to heterogeneous cellular states across cell types and patients, and supports our transcriptomic and functional data elucidating AP-1 induction to be a key neural vulnerability hijacked by PCY-hit NADs.

Preclinical translation of neuroactive drugs

Vortioxetine elicits a strong Ca^{2+} influx and subsequent AP-1 response, reduces aggressive GSC morphologies, and potently induces cell death of glioblastoma cells *ex vivo*. To determine if Vortioxetine affects other tumor properties that contribute to recurrence such as invasiveness and long-term growth, we performed a series of experiments to test the effect of Vortioxetine on cell invasion, clonogenic survival, and spheroid formation using established human long-term glioma cell lines (LN-229, LN-308) and glioma-initiating cells (ZH-161, ZH-562) (Extended Data Fig. 9c-f). In a collagen-based spheroid invasion assay, Vortioxetine decreased the average migration distance and reduced the number of invading cells in 3 out of 4 lines (Extended Data Fig. 9c,d). In a resazurin-based clonogenic survival assay, Vortioxetine strongly impaired long-term cell viability in a concentration-dependent manner across all cell lines (4 out of 4 lines, Extended Data Fig. 9e). In a complementary 3D spheroid-formation assay, Vortioxetine potently inhibited tumor growth over time (Extended Data Fig. 9f). These results demonstrate the multifaceted anti-tumor effects of Vortioxetine upon glioblastoma invasion, survival, and proliferation.

Finally, we tested the top *ex vivo* NAD hits including Vortioxetine (PCY-hit NADs; n=4 or 5 drugs across different drug classes) in orthotopic human-xenograft glioblastoma mouse models (Fig. 5f and Extended Data Fig. 10a-c). To account for the variability observed in different orthotopic models, we tested two different models (LN-229, ZH-161) across three independent trials (Trials I-III) of drug-testing *in vivo* (Fig. 5f and Extended Data Fig. 10a). We included Temozolomide (TMZ) as a positive control, and as negative controls we tested one PCY-neg NAD Paliperidone and a vehicle control. Since all tested NADs have confirmed BBB-penetrance and are approved for other neurological disorders, *in vivo* concentrations were determined *a priori* based on literature and clinical evidence [68–73]. Vortioxetine was consistently the most effective drug (in 3/3 trials) and showed significant survival benefit comparable to TMZ despite being tested at considerably lower dosage (Fig. 5f). Brexpiprazole was the 2nd-best PCY-hit NAD *in vivo* (2/3 trials), while other NADs showed a significant survival benefit in 1 out of 3 trials (Extended Data Fig. 10a). Consistent with PCY, the negative control Paliperidone did not show a significant survival benefit (2/2 trials) (Fig. 5f). In the most aggressive orthotopic model with the shortest median survival of the vehicle control, Vortioxetine and TMZ were the only effective drugs (Trial II: ZH-161; Fig. 5f, right), whereas for the least aggressive model, all tested PCY-hit NADs (5/5 NADs) significantly prolonged survival (Trial III: ZH-161; Extended Data Fig. 10a). MRI images of ZH-161 transplanted mice (Trial II) after 15 days of Vortioxetine, Apomorphine, and Temozolomide treatment showed marked reduction of tumor size (Extended Data Fig. 10b,c). The striking consistency of our patient *ex vivo* and mouse *in vivo* results demonstrate strong translatability of PCY-based NAD discovery and confirm Vortioxetine as the most promising clinical candidate.

Given the different mechanisms of neuroactive drugs and approved chemotherapies, their successful combination could facilitate the rapid adoption of NADs into clinical routine. Therefore, we tested the combination of Vortioxetine with either first- or second-line standard of care drugs for glioblastoma, TMZ and Lomustine (CCNU) *in vivo* (Trial IV: ZH-161; Fig. 5g). All three single agents significantly prolonged survival, with Vortioxetine results now confirmed in 4 out of 4 *in vivo* trials (Fig. 5f,g). Remarkably, compared to TMZ or CCNU single agents, the combination of Vortioxetine with either

drug provided even further survival benefit, with a median survival increase of 20-30% compared to the single agents (Fig. 5g). Given the dire need for effective treatment options in glioblastoma, this strong preclinical evidence of the safe antidepressant Vortioxetine urges for clinical investigation in patients.

Discussion

Here we present the first therapeutic single-cell map across glioblastoma patient samples that reveals the morphological and neural molecular heterogeneity of glioblastoma. Glioblastoma stem cells adopt distinct cell morphological states that encode clinical prognostic value. While the presence of tumor microtubes has been associated with tumor grade [2], we show that even within glioblastoma, complex GSC morphologies are prognostic of shorter progression-free survival. Image-based drug screening in the context of heterogeneous patient samples predicted clinical response to chemotherapy and enabled the discovery of repurposable neuroactive drugs that target the spectrum of glioblastoma cells across 27 patients and various model systems, greatly expanding upon prior literature [74–76].

A number of new personalized therapeutic opportunities emerge from our exploratory drug response analysis across a genetically and clinically heterogeneous patient cohort. These include Elesclomol sensitivity increasing with age, Abemaciclib response associating with p53 mutant status, and higher Brexpiprazole response in men. Response to the antidepressant Vortioxetine, the most promising preclinical candidate, was particularly aligned with aggressive GSC morphotypes present in patients with poor prognosis. These efforts contribute to the nascent community of glioblastoma research focusing on the investigation of patient-derived tumor explants that facilitate translational investigation of complex tumor behavior, including the development of genetically characterized patient cultures, organoid biobanks, and regionally annotated samples [29,77–82].

Our systematic analysis of the neuroactive drug mechanisms, drug target expression, and functional genetic dependencies indicated a diverse set of possible neural vulnerabilities of glioblastoma. Given this diversity, it is surprising that our interpretable machine learning approach COSTAR identified a simple drug-target connectivity signature predictive of anti-glioblastoma efficacy. COSTAR effectively applies Occam's razor to the collective biochemical drug-protein-protein interaction networks, offering a novel conceptual framework applicable to all fields of drug discovery. Through COSTAR, we uncovered a convergence of AP-1 transcription factor activity and cell cycle regulation on BTG-mediated tumor suppression. AP-1 and BTG upregulation was a defining feature of the response to neuroactive drugs with anti-glioblastoma activity, where a growth-suppressing role for BTG1 was confirmed by functional genetics. While the defining pharmacological properties remain to be identified, our results indicate a plurality of drug mechanisms converging on this novel tumor-suppressing pathway.

Previous studies have demonstrated the role of neuronal activity in regulating glioblastoma growth at the brain-tumor interface, highlighting the influence of the tumor microenvironment in mediating the neural behavior of the tumor. Here we reveal that cell-*intrinsic* neural activity in glioblastoma mimics those of neural lineage cells, offering a therapeutic vulnerability that enables direct targeting of the tumor. In neurons, immediate early gene expression including AP-1 is typically a hallmark of neural activity or insult, but in cancer cells, AP-1 factors were originally described as context-dependent oncogenes. We now find that neuroactive drugs can hijack this activity-dependent neural signaling, triggering a strong transcriptional response that, in the context of glioblastoma cells, leads to rapid cell

505 death. Treating glioblastoma tailored to the cellular history and lineage of the cancer rather than its
506 unstably transformed state may represent new hope for this devastating disease.

507 Acknowledgements

508 We thank the patients and their families for making this study possible. We thank core facilities at ETH
509 Zurich and University of Zurich, including the Functional Genomics Center Zurich (FGCZ), the Flow
510 Cytometry Core Facility (EPIC, FCCF), and central informatics services (ID). This project has received
511 funding from the European Research Council (ERC) under the European Union's Horizon 2020 research
512 and innovation programme (Grant agreement No. 803063-SCIPER; BS), and from the Personalized
513 Health and Related Technologies (PHRT) Strategic Focus Area of the ETH Domain (Project #2021-566;
514 BS). We further acknowledge funding from the European Union/European Commission (MSCA
515 Individual Fellowship; SL), the European Molecular Biology Organization (EMBO Long-term Post-
516 doctoral Fellowship; SL), the Swiss National Science Foundation (grant no. 310030_204972; MAH), and
517 financial support from the Department of Biology as well as the Institute of Molecular Systems Biology
518 of the ETH Zurich. We thank the research and administrative staff who helped us throughout the study,
519 including Yasmin Festl and Silas Krämer, and members of the Snijder lab for discussions.

Figure 1

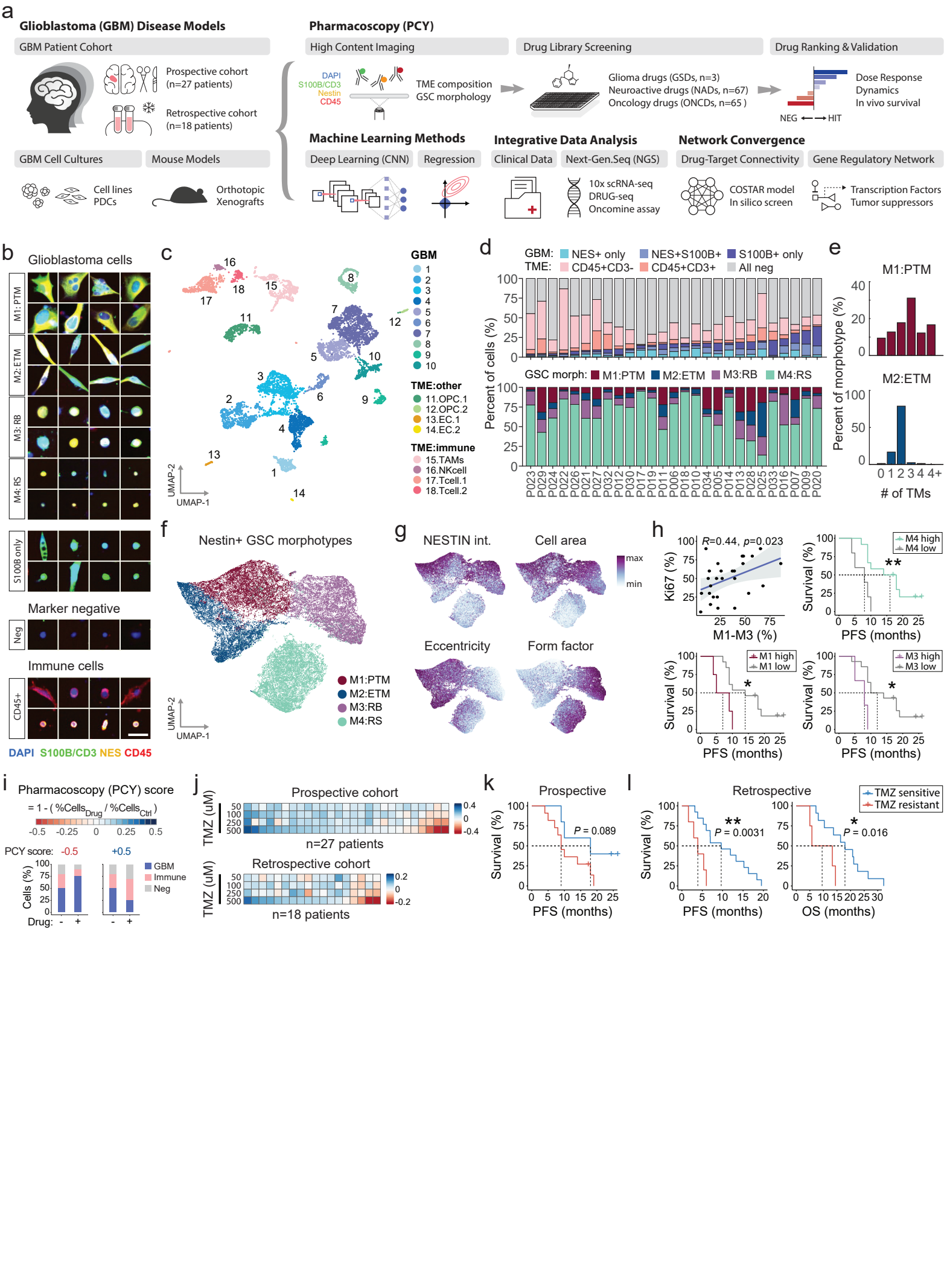

Figure Legends

Fig. 1: Neural intratumor heterogeneity across glioblastoma patients relates to disease prognosis and response to first-line therapy

a, Comprehensive workflow integrating glioblastoma disease models with image-based *ex vivo* drug screening (pharmacoscopy; PCY), machine learning methods, clinical data, and next-generation sequencing (NGS) to discover therapeutic neural vulnerabilities underlying glioblastoma. Glioblastoma disease models include surgery material from glioblastoma patient samples (prospective cohort; n=27 patients, retrospective cohort; n=18 patients), patient-derived lines (PDCs, n=3 lines), glioblastoma cell lines (n=4 lines), and mouse models (n=2 human xenograft models). Different cell types present in the tumor microenvironment (TME) of glioblastoma patient samples are identified by both immunofluorescence (S100B, Nestin, CD3, CD45, DAPI) and single-cell RNA-Seq (10x). Glioblastoma stem cell (GSC; Nestin+ cells) morphologies are classified into four morphotypes by deep learning (convolutional neural network; CNN). Pharmacoscopy measures the relative changes in TME composition and GSC morphotypes across drug treatments to identify drugs with anti-glioblastoma efficacy (PCY-hit). Drug-target connectivity mapping of PCY-hit drugs by a novel machine learning method (convergence of secondary drug-targets by analyzed by regularized regression; COSTAR) together with multiplexed RNA-Seq (DRUG-Seq) enables the discovery of convergent gene regulatory networks involved in glioblastoma suppression. **b,** Compositional and morphological diversity of glioblastoma patient samples are captured with single-cell resolution by high-content imaging. Glioblastoma cells (Nestin+ or S100B+) include S100B only cells (S100B+Nestin-CD45-) and four Nestin+CD45- GSC morphotypes: M1 polygonal multi-tumor microtube cells (M1:PTM), M2 elongated uni/bi-tumor microtube cells (M2:ETM), M3 round big cells (M3:RB), and M4 round small cells (M4:RS). Other cell types include immune cells (CD45+ only, CD45+CD3+) and marker-negative cells. Scale bar, 30µm. **c,** UMAP projection of 7684 single-cell transcriptomes from four glioblastoma patient samples (P007, P011, P012, P013) colored by cluster-id (see legend). Clusters are based on Leiden community detection and cell types assigned by marker expression (*Extended Data Figure 1f*). Glioblastoma (GBM) clusters (1-10) are numbered in descending order based on cluster-averaged expression of the Gene Ontology term “stem cell differentiation” (GO:0048863). OPC; oligodendrocyte precursor cells. EC; endothelial cell. TAM; tumor-associated macrophage. NK; natural killer cell. TME; tumor microenvironment. **d,** Cellular (top) and morphological (bottom) composition across the prospective glioblastoma cohort (n=27 patients; columns). Cellular composition is based on glioblastoma and TME populations defined by marker expression and morphological composition is based on Nestin+ GSCs classified by deep learning into four morphotypes (M1-M4). **e,** Frequency of tumor microtubes (TMs) per cell in TM-containing morphotypes M1 (n=180 cells) and M2 (n=264 cells). **f-g,** UMAP projection of the morphological CNN feature space of 84,180 single-cells (up to n=1000 cells per morphotype and patient, n=27 patients). CNN feature space consists of ten-dimensional activations taken from the 2nd-last fully connected layer of the network. **f,** Cells are colored by their assigned morphotype (M1-M4). **g,** Cells are colored by the local median of selected single-cell features (see also *Extended Data Figure 2c*). Eccentricity and form factor are shape indices related to the irregularity and circularity of a cell. Nestin Int.; Nestin expression measured by immunofluorescence. **h,** (Top left) Correlation of histopathological Ki67 labeling index with abundance of M1-M3 morphotypes per patient. Linear regression line (dark blue) with a 95% confidence interval (light grey). Pearson correlation coefficient R=0.44, *P*-value 0.023. (Top right and bottom panels) Morphotype abundance-based stratification of

progression-free survival (PFS) in primary glioblastoma patients (n=17 patients) plotted as Kaplan-Meier survival curves. (Top right) M4-high; n=12, M4-low; n=5 patients; *P*=0.0047. (Bottom left) M1-high; n=4, M1-low; n=13 patients; *P*=0.021. (Bottom right) M3-high; n=3, M3-low; n=14 patients; *P*=0.018. **i,** Schematic illustrating pharmacoscopy (PCY) score calculation. The PCY score quantifies drug-induced on-target killing by measuring the change in fraction of a defined target population (blue; relative reduction, red; relative increase) compared to vehicle control (-). Bar plot example of two opposing cases scoring a relative 50% decrease (score=0.5) or relative 50% increase (score -0.5) of glioblastoma cells in response to a drug. **j,** Temozolomide (TMZ) *ex vivo* drug response across four TMZ concentrations 50, 100, 250, and 500µM (rows) per patient (columns) for two patient cohorts (top: prospective cohort, n=27 patients; bottom: retrospective cohort, n=18 patients). Heatmap color scale indicates the PCY score of glioblastoma cells (Nestin+ or S100B+). Outliers beyond color scale limits were correspondingly set to minimum and maximum values. **k-l,** Temozolomide (TMZ) *ex vivo* sensitivity-based stratification of primary glioblastoma patient survival plotted as Kaplan-Meier curves. All patients received TMZ as 1st-line treatment in the clinic with censored patients in the prospective cohort indicating ongoing responses (tick marks). *Ex vivo* TMZ sensitivity is calculated as the mean PCY score across four TMZ concentrations 50, 100, 250, and 500µM. **k**, Progression-free survival (PFS) of the prospective glioblastoma cohort (n=16 patients; *P*=0.089). **l,** Progression-free survival (PFS; *P*=0.0031; left) and overall survival (OS; *P*=0.016; right) of the retrospective validation cohort (n=18 patients). **h,k-l,** Survival curves are compared using the log-rank (Mantel-Cox) test and the optimal cut-point (high, low) for continuous parameters to stratify patients was determined by maximally selected rank statistics. *P*-values: not significant (ns), $P > 0.05$, *$P < 0.05$, **$P < 0.01$, ***$P < 0.001$, ****$P < 0.0001$.

Figure 2

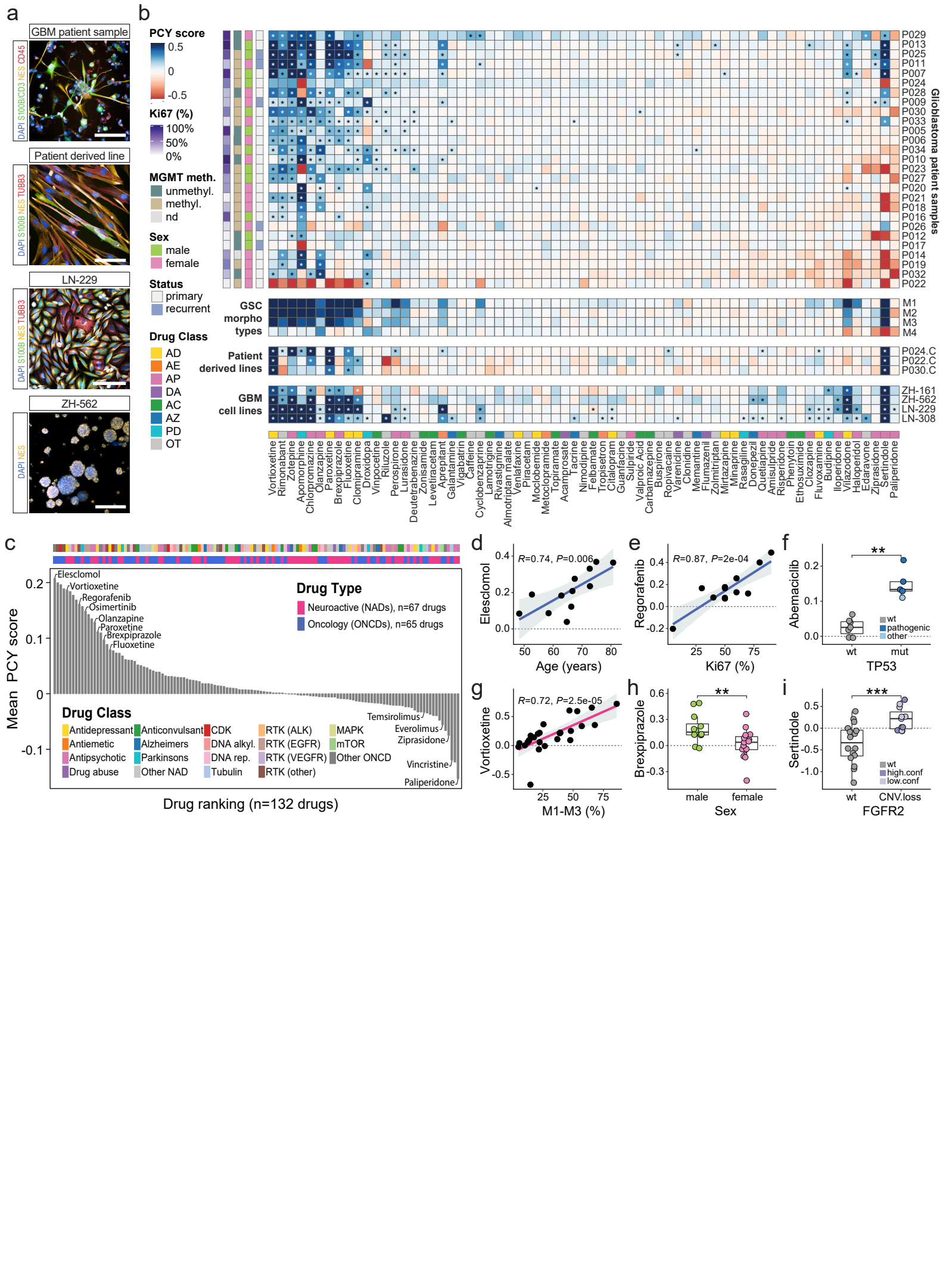

Fig. 2: Image-based single-cell drug profiling across a heterogeneous patient cohort and model systems identifies repurposable drugs for glioblastoma treatment

a, Representative immunofluorescence images of a glioblastoma patient sample (P040; scale bar, 100µM), a patient-derived cell line (P040.PDC; 100µM), an adherent glioblastoma cell line (LN-229; scale bar, 150µm), and a glioblastoma-initiating cell line (ZH-562, scale bar, 250µm). Cells are labeled with the nuclear stain DAPI (blue), mature astrocyte marker S100B (green), and neural progenitor marker Nestin (yellow). Other markers are indicated in their respective colors. **b,** Drug response matrix of neuroactive drugs (NADs, n=67 drugs) across glioblastoma patient samples (n=27 patients), GSC morphotypes (n=4 classes), patient-derived lines (PDCs; n=3 lines, denoted by ".C" following patient id), and glioblastoma cell lines (n=4 lines). Heatmap color scale indicates the PCY score of glioblastoma cells (defined as Nestin+ or S100B+ cells in patient samples; Nestin+ cells in PDCs; total cell number in LN-229/308 lines; spheroid area in ZH-161/562 lines) or the average PCY score of GSC morphotypes (M1-M4) across patients. Outliers beyond color scale limits were correspondingly set to minimum and maximum values. Annotations per patient sample (rows; left of heatmap) indicate the clinical parameters Ki67 labeling index, MGMT promoter methylation status (unmethyl; unmethylated, methyl; methylated, nd; not determined), Sex, and recurrent tumor status (Status). *See also Extended Data Figure 1a and Supplementary Table 2 for tumor mutational status*. Annotation per drug (columns; underneath heatmap) indicates neuroactive drug class. Asterisks (*) denote FDR-adjusted $P < 0.05$. **c,** Drug ranking (n=132 repurposable drugs) according to their mean Nestin+ or S100B+ PCY scores across glioblastoma patients (NADs; n=27 patients, ONCDs; n=12 patients). Annotations per drug indicate drug type (NADs; n=67 drugs, ONCDs; n=65 drugs) and drug class. RTK; receptor tyrosine kinase, alkyl; alkylation, rep; replication. **d-i** Genetic and clinical associations with *ex vivo* drug response across patients. Glioblastoma PCY scores (y-axis) are plotted per patient against selected parameters (x-axis). **d,** Correlation of patient age at diagnosis with *ex vivo* Elesclomol response (R=0.74; $P = 0.006$). **e,** Correlation of histopathological Ki67 labeling index with *ex vivo* Regorafenib response (R=0.87; $P = 0.0002$). **f,** Association of *TP53* mutational status with *ex vivo* Abemaciclib response ($P = 0.0025$). **g,** Correlation of complex GSC morphotype abundance (M1-M3) at baseline with *ex vivo* Vortioxetine efficacy. **h,** Association of sex with *ex vivo* Brexpiprazole response ($P = 0.0063$). **i,** Association of *FGFR2* copy number loss with *ex vivo* Sertindole response ($P = 0.0008$). CNV; copy number variation. High.conf; high confidence. Low.conf; low confidence. *See Extended Data Figure 3f,g for full pharmacogenetic analysis results.* **d,e,g,** Linear regression line with a 95% confidence interval. Pearson correlation coefficients with *P*-values annotated. **f,h,i,** *P*-values calculated from a two-sided Wilcoxon rank sum test. *P*-values: not significant (ns), $P > 0.05$, *$P < 0.05$, **$P < 0.01$, ***$P < 0.001$, ****$P < 0.0001$. Boxplots show 25th–75th percentiles with a line at the median; whiskers extend to 1.5 times the interquartile range.

Figure 3

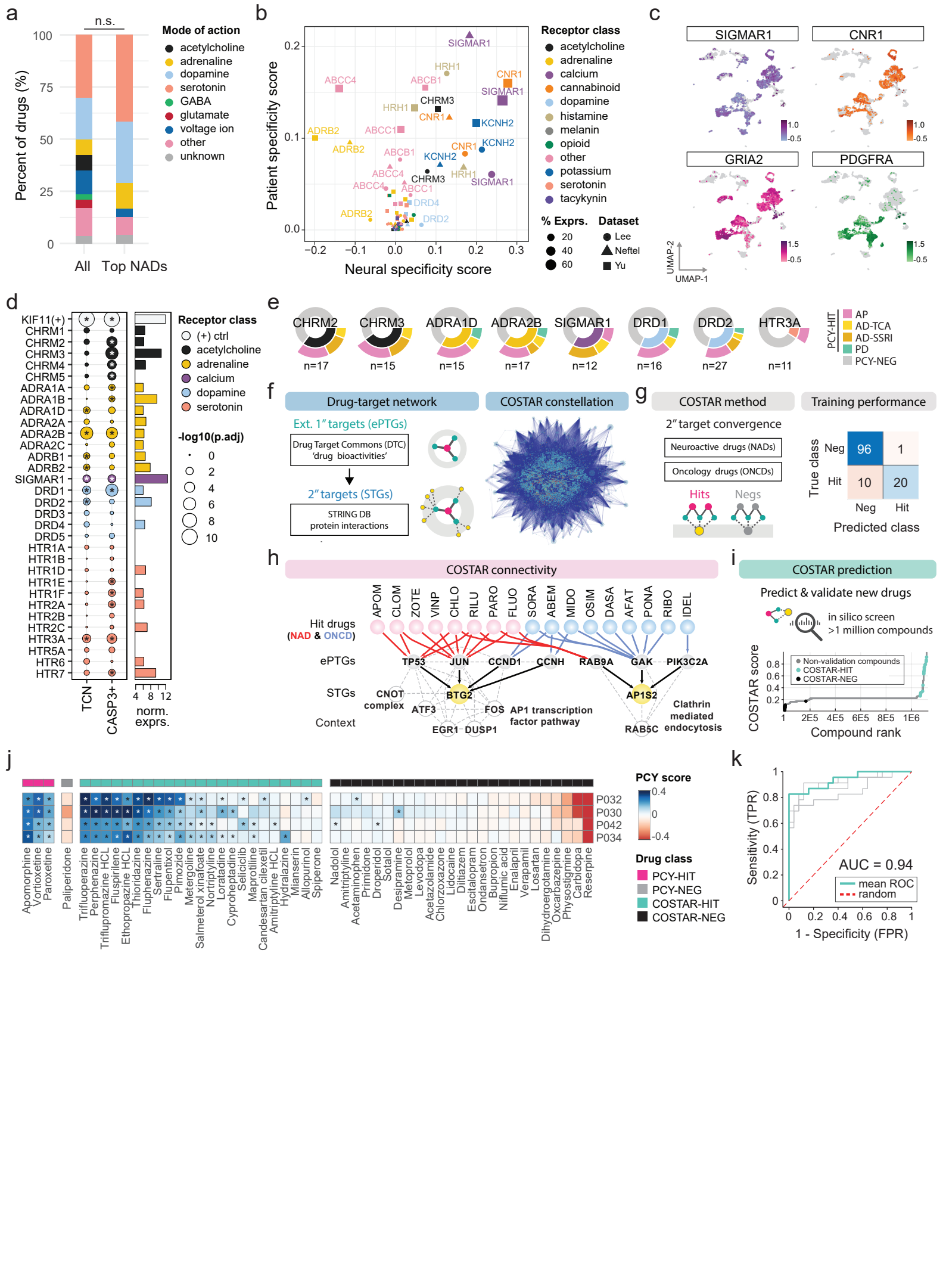

Fig. 3: Neuroactive drugs with anti-glioblastoma efficacy converge upon a predictive AP-1 and cell cycle connectivity signature through divergent primary targets

a, Drug mode-of-action for all neuroactive drugs (n=67 drugs; left) and top neuroactive drug hits (n=15 drugs with a mean patient PCY score > 0.03; right) represented as stacked bar plots. Hypergeometric test shows no enrichment in mode-of-action: n.s., not significant. **b,** Primary target gene (PTG) expression of neuroactive drugs in 22 glioblastoma patient samples across three independent scRNA-Seq datasets (Lee *et al.*, this study; n=4 patients, n=7684 cells; Neftel *et al.*, n=9 patients, n=13519 cells; Yu *et al.*, n=9 patients, n=4307 cells) plotted as the neural specificity score (x-axis) versus patient specificity score (y-axis) for each PTG. *See also Extended Data Figure 5b & Methods*. Each dot represents a gene, shape corresponds to the dataset, and size scales with percent of expressed cells. Color represents the receptor class of each PTG. **c,** scRNA-Seq log10(expression) of selected neuroactive PTGs (*SIGMAR1*, *CNR1*, *GRIA2*) and oncogenic RTK (*PDGFRA*) visualized on a UMAP projection of 7684 single-cell transcriptomes (Lee *et al.*, this study, n=4 glioblastoma patients). **d,** siRNA-mediated gene silencing of PTGs in LN-229 cells. Total cell number reduction (TCN) and cleaved CASP3+ fraction increase (CASP3+) depicted as a circle per gene. Circle sizes scale with the –log10 (FDR-adjusted P-value) and color represents the receptor class of each PTG. S*ee also Extended Data Figure 5c,d for additional receptor classes and PCY scores*. Adjacent horizontal bar plot represents baseline expression (DESeq2 vsd-normalized RNA-Seq counts) of each PTG in LN-229 cells. Asterisks (*) denote FDR-adjusted $P < 0.05$. **e,** Fraction of PCY-HIT vs PCY-NEG drugs associated with PTGs based on the Drug Target Commons (DTC) [52], where the number of drugs (n) denotes drugs with annotations for a given gene. Representative PTGs with the strongest glioblastoma gene dependencies of each receptor class visualized. Inner circle color corresponds to receptor class in *Figure 3d* for PCY-HIT drugs, while PCY-NEG drugs are in grey. PCY-HIT drugs are subdivided and colored according to their drug class. AP; antipsychotic, AD-TCA; antidepressant -tricyclic, AD-SSRI; antidepressant-selective serotonin reuptake inhibitor, PD; Parkinson's disease. **f,** Convergence of secondary drug targets analyzed by regularized regression (COSTAR). For all tested drugs, the extended primary targets (ePTG; Ext. 1'') were retrieved from DTC, and expanded to include secondary targets (STG; 2'') based on protein-protein interactions annotated by STRING-DB [83] (left). The resulting network, or 'COSTAR constellation' (right), contains 127 drugs, 975 ePTGs, 10573 STGs, and 114517 edges. **g,** Logistic LASSO regression is performed on the COSTAR constellation to learn a linear model that discriminates pharmacoscopy hits (n=30, equally split across NADs and ONCDs) from negative drugs (n=97) based on their secondary drug-target connectivity (left). COSTAR training model performance is represented as a confusion matrix, where the 'true' class denotes PCY-based experimental ground truth, and the 'predicted' class denotes the COSTAR-prediction (right). **h,** COSTAR connectivity (solid lines) reveals convergence of NAD (red) and ONCD (blue) hits to key ePTGs (grey) and STGs (yellow). See *Extended Data Figure 6b* for the full model. Representative proteins/protein families with high confidence STRING-DB interactions to STGs are shown as context (dashed lines). **i,** *In silico* COSTAR predictions based on drug-target connectivity across 1,120,823 drugs annotated in DTC. Drugs are ranked (x-axis) by their predicted PCY-hit probability (COSTAR score; y-axis). Predicted drug hits (COSTAR-HIT; mint green) and predicted non-hits (COSTAR-NEG; black) selected for experimental validation are indicated. **j,** Experimental validation of COSTAR-HIT (n=23; mint green) and COSTAR-NEG (n=25; black) drugs (columns) across four glioblastoma patient samples (rows). Heatmap color scale indicates the PCY score of glioblastoma cells. Additionally, positive (PCY-HITs; pink; n=3) and negative (PCY-NEG; dark grey; n=1) control drug responses are shown. Outliers beyond color scale limits were correspondingly set to minimum and maximum values. Asterisks (*) denote FDR-adjusted $P < 0.05$. **k,** Receiver Operating Characteristic

(ROC) curves describing the COSTAR validation accuracy in glioblastoma patient samples of the COSTAR-predicted drugs (n=48 drugs). ROC curves per patient sample (grey, n=4 patients) and mean across all patients (mint green) and corresponding Area Under the Curve (AUC) are shown. Dashed red line denotes the ROC curve of a random classifier. Patient drug responses correspond to *Figure 3j*.

Figure 4

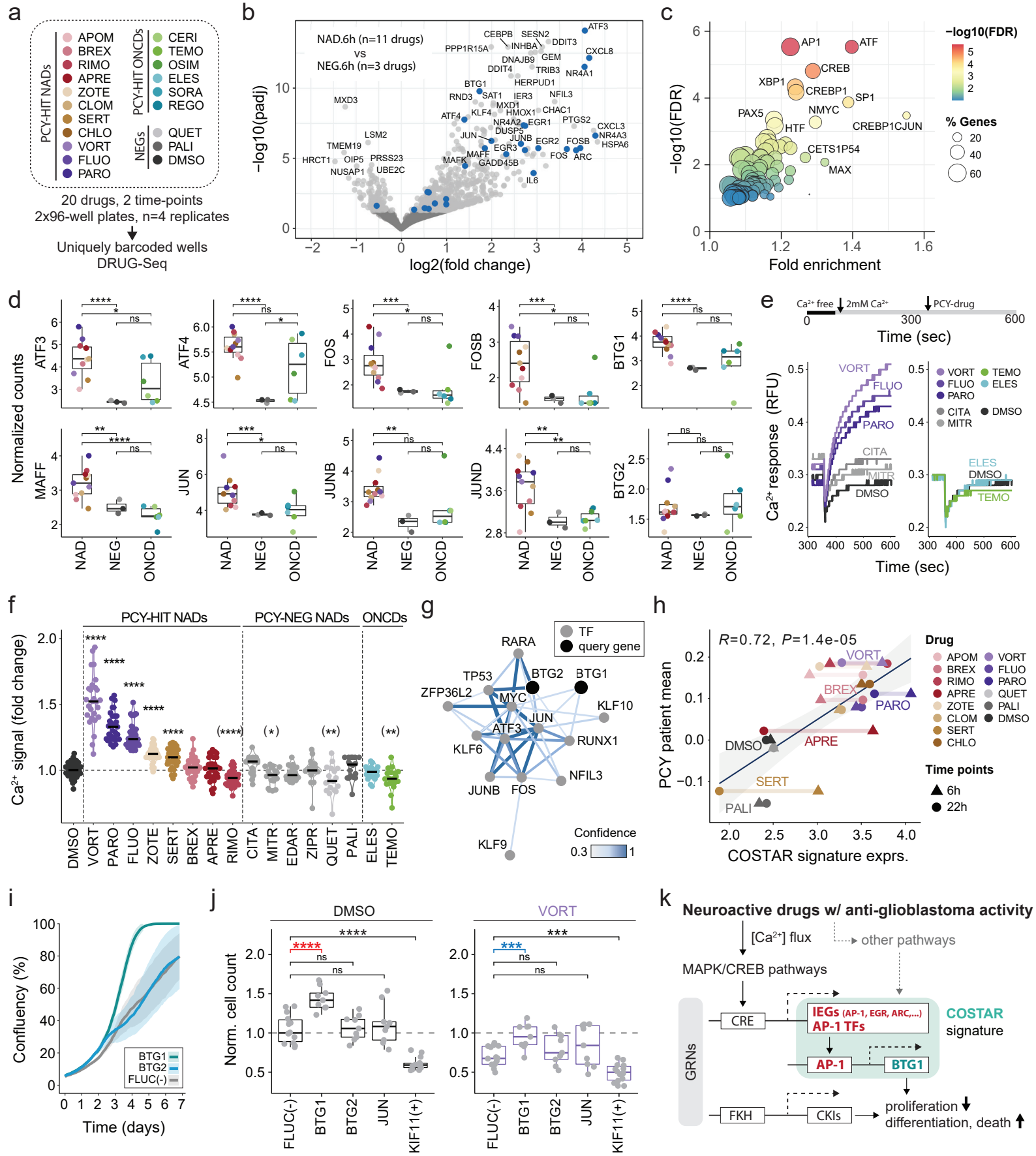

Fig. 4: Glioblastoma suppression is driven by a tumor-intrinsic AP-1 gene regulatory network upon neural activity

a, Multiplexed RNA-Seq (DRUG-Seq) measures the transcriptional response to pharmacoscopy-hit neuroactive drugs (PCY-hit NADs, n=11 drugs), pharmacoscopy-hit oncology drugs (PCY-hit ONCDs, n=6 drugs), and negative control drugs (NEGs, n=2 PCY-neg NADs and DMSO vehicle control). LN-229 cells were treated with drugs across two different time-points (6, 22 hours) and uniquely barcoded for sequencing (n=4 replicate wells per drug). **b**, Transcriptional response of PCY-hit NAD-treated cells compared to NEG-treated cells(6h) shown as a volcano plot. X-axis: log2(fold change); y-axis: –log10(adjusted *P*-value). A positive log2(fold change) indicates upregulated genes upon PCY-hit NAD treatment. Genes above a –log10(0.05 adjusted P-value) threshold plotted as light grey dots, and non-significant genes as dark grey dots. Highlighted genes (blue) include AP-1 transcription factor (TF) network genes (Pathway Interaction Database; PID AP1 PATHWAY; [84]) and key COSTAR signature genes. **c**, Transcription factor binding site enrichment analysis of significantly upregulated genes upon PCY-hit NAD treatment (6 hours) in *Figure 4b*. Circles correspond to TF annotations, circle sizes scale with the percent of genes present in the annotation, and colors indicate –log10(false discovery rate). **d**, Expression of AP-1 TF and BTG family genes that are significantly upregulated upon PCY-hit NAD treatment compared to negative controls (6 hours) plotted as DESeq2 vsd-normalized RNA-Seq counts (y-axis). Box plot groups correspond to drug categories and dots represent the average expression per drug. Drug categories 'PCY-hit NAD' and 'PCY-hit ONCD' abbreviated to NAD and ONCD, respectively. Two-sided t-test. Significant *P*-values in order of appearance per gene: *ATF3*, *P*=1.1e-05, *P*=0.039; *ATF4*, *P*=7.8e-08, *P*=0.036; *FOS*, *P*=0.0005, *P*=0.035; *FOSB*, *P*=0.0006, *P*=0.01; *BTG1*, *P*=9.3e-06; *MAFF*, *P*=0.0053, *P*=8.3e-05; *JUN*, *P*=0.0006, *P*=0.023; *JUNB*, *P*=0.0025; *JUND*, *P*=0.0023, *P*=0.0013. **e**, Calcium response over baseline of LN-229 cells upon drug treatment measured by high-throughput FLIPR assay. (Top) Timeline depicts assay setup, where cells were treated with their respective PCY-drug after equilibration in 2mM calcium-containing buffer. (Bottom) Among 17 tested conditions, representative traces following drug treatment from 8 conditions including 5 antidepressants on the left panel (PCY-hit NADs: VORT/FLUO/PARO; PCY-neg NADs: CITA/MITR), and 2 ONCDs on the right panel (PCY-hit ONCDs, ELES/TEMO). DMSO vehicle control traces shown in both. RFU; relative fluorescence units. **f**, Fold change in extracellular calcium influx upon drug treatment relative to DMSO vehicle control measured by FLIPR assays in LN-229 cells (n=8 assay plates; n=17 conditions; n=18-30 wells/drug; DMSO, n=47 wells). Normalized calcium levels for each drug were calculated by averaging calcium levels after drug treatment (400-600 seconds interval) divided by the basal level of calcium prior to drug administration (200-300 seconds interval) where experimental time corresponds to *Figure 4e*. Different drug categories including PCY-hit NADs, n=8 drugs; PCY-neg NADs, n=6 drugs; PCY-hit ONCDs, n=2 drugs were compared. Two-sided t-test against DMSO vehicle control. *P*-values adjusted for multiple comparisons by Holm correction. *P*-values: VORT, n=27, *P*=2.4e-26; PARO, n=29, *P*=9.1e-27; FLUO, n=30, *P*=3.2e-23; ZOTE, n=30, *P*=2.9e-12; SERT, n=30, *P*=6.5e-07; RIMO, n=30, *P*=8.3e-05; MITR, n=18, *P*=3.2e-02; QUET, n=18, *P*=2.2e-03; TEMO, n=18, *P*=2.5e-03. Asterisks in parentheses denote drug treatment conditions where the median [Ca2+ fold change] < 0. Black line indicates the median value. **g**, Transcriptional regulation of BTG1/2 based on PathwayNet [67]. Query genes (*BTG1/2*, black nodes) and the top-13 inferred transcription factor interactions (grey nodes) are shown. Color of network edges indicates relationship confidence (see colorbar). **h**, Correlation of COSTAR signature expression (x-axis) with *ex vivo* patient neuroactive drug response (y-axis) plotted per drug (color) and time-point (shape). Mean glioblastoma PCY score across patients (n=27 patients, prospective cohort) of neuroactive drugs (n=11 PCY-H NADs, n=3 NEGs) plotted against their corresponding geometric

mean expression of AP-1 TFs and *BTG1/2* genes measured by DRUG-seq as shown in *Figure 4d*. Linear regression line (black) with a 95% confidence interval (light grey). Pearson correlation coefficient R=0.72, *P*-value 1.4e-05. **i,** Confluency of LN-229 cells measured by IncuCyte live-cell imaging (y-axis) across seven days (x-axis) in two siRNA knockdown conditions (*BTG1*, *BTG2*) and a negative firefly luciferase control (*FLUC*). Mean of n=4 replicate wells shown with +/- one standard deviation. **j**, Effect of target gene siRNA knockdown (columns) on LN-229 viability (y-axis) at baseline (DMSO; left panel) and upon Vortioxetine treatment (VORT; 10µM; right panel). Knockdown of kinesin-like motor protein *KIF11* used as a positive (+) control. Cell count normalized (norm. cell count) to the *FLUC* negative (-) control siRNA within each experiment (n=9-14 replicate wells/condition, n=2 experiments). Two-sided t-test. *P*-values adjusted for multiple comparisons by Holm correction. *P*-values: DMSO; *BTG1* vs *FLUC*, *P*=6.99e-05; *KIF11* vs *FLUC*, *P*=3.33e-08. VORT; *BTG1* vs *FLUC*, *P*=0.0008; *KIF11* vs *FLUC*, *P*=0.0006. **k**, Pathway diagram summarizing mechanistic pathways by which neuroactive drugs target glioblastoma. GRN; gene regulatory network. IEG; immediate early gene. CKI: cyclin-dependent kinase inhibitor. CRE; cAMP response element. FKH; forkhead binding motif. **a,d-f,h,** Colors correspond to drugs and drug name abbreviations annotated in *Supplementary Table 3*. *P*-values: not significant (ns), $P > 0.05$, *$P < 0.05$, **$P < 0.01$, ***$P < 0.001$, ****$P < 0.0001$. Boxplots show 25th–75th percentiles with a line at the median; whiskers extend to 1.5 times the interquartile range.

Figure 5

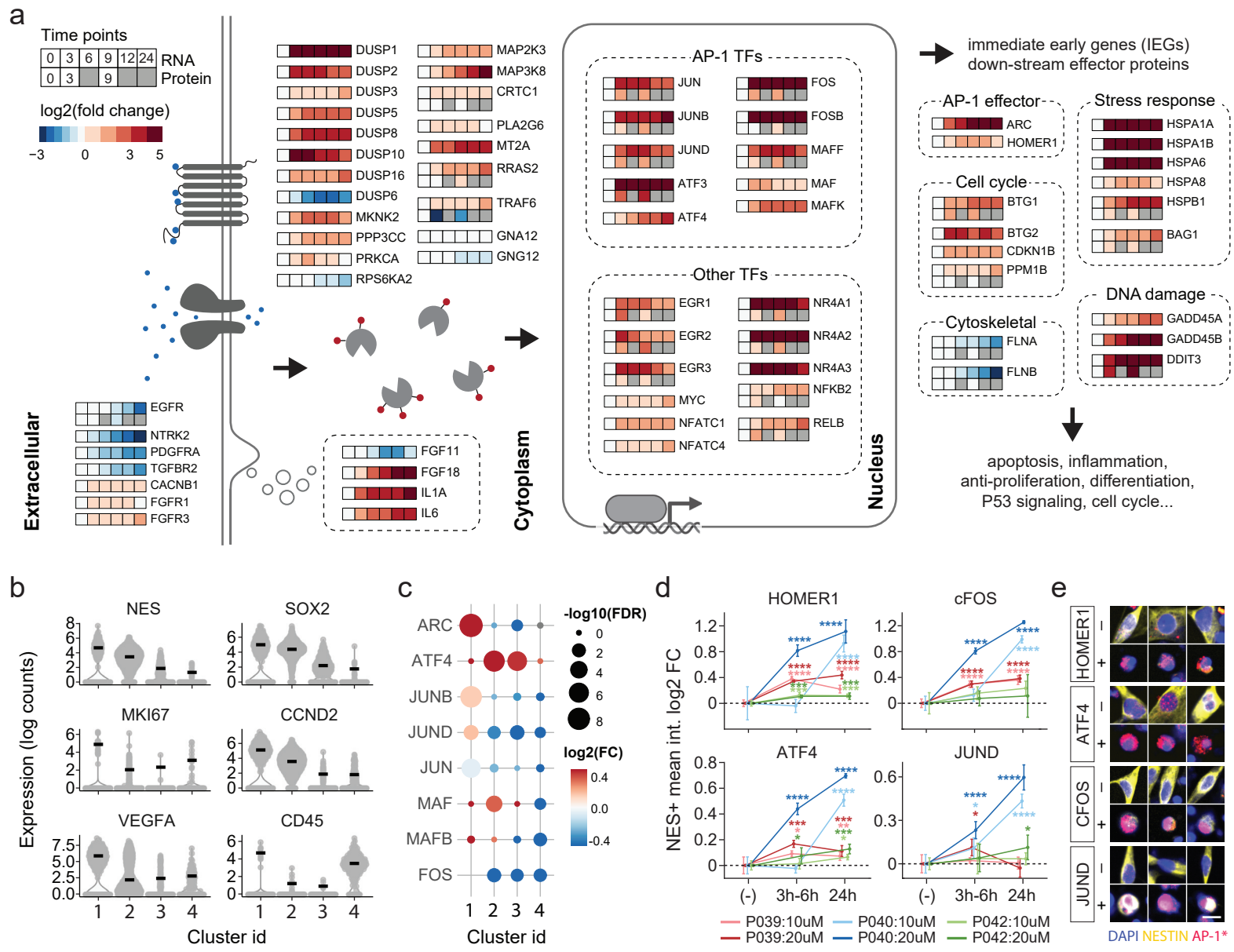

Fig. 5: The antidepressant Vortioxetine induces a potent AP-1 response that synergizes *in vivo* with current standard of care drugs for glioblastoma

a, Time-course visualization of AP-1 (PID) and MAPK (KEGG) pathway induction following Vortioxetine treatment (20µM) in LN-229 cells. Six time-points were measured by RNA-Seq and three time-points by proteomics (n=3 replicates/time-point). Genes selected for visualization are significantly differentially expressed by RNA-Seq at all time-points compared to the first time-point (0h). Heatmap color scale represents log2(fold change) compared to the 0h time-point. **b,** scRNA-Seq expression log2(UMI) of selected glioblastoma and top cluster marker genes from glioblastoma patient sample P024. Cluster ids are based upon UMAP clustering of both DMSO and Vortioxetine (VORT, 20µM) treated cells (3h) shown in *Extended Data Figure 9a*. Black lines indicate the median value. **c,** Differentially expressed AP-1 transcription factors and downstream effector gene ARC per scRNA-Seq cluster upon VORT treatment compared to DMSO in P024. Circle sizes scale with the –log10 (adjusted *P*-value) and heatmap color scale represents VORT-induced log2(fold change) compared to DMSO treated cells per cluster. **d,** Induction of AP-1 transcription factors and downstream effector gene *HOMER1* in glioblastoma patient samples (n=3 additional patients; P039, P040, P042) upon Vortioxetine treatment in Nestin+ cells. Immunofluorescence measurements across different time-points (3-6 and 24 h) and different Vortioxetine concentrations (10, 20µM). **e,** Representative single-cell image crops from glioblastoma patient P040 of Nestin+ cells stained with different AP-1 transcription factors and downstream effector gene HOMER1 after Vortioxetine treatment (+; 20µM) and DMSO vehicle control (-) at 24 hours. Cells are pseudo-colored with DAPI (blue), Nestin (yellow) and AP-1 transcription factors/HOMER1 (red). Two-sided t-test compared to negative control. Scale bar, 15µm. **f,** Survival analysis of Trial I: LN-229 (left) or Trial II: ZH-161 (right) tumor-bearing mice (n=6-7 mice per group). Mice were treated intraperitoneally (*i.p.*) between days 5-21 after tumor implantation with a PCY-HIT NAD, Vortioxetine (VORT; 10mg/kg; Trial I, *P*=0.0001; Trial II, *P*=0.0016), a positive control, Temozolomide (TMZ; 50mg/kg; Trial I, *P*=0.0009 ; Trial II, *P*=0.0002), a PCY-NEG NAD, Paliperidone (PALI; 5mg/kg), and a negative vehicle control. *See also Extended Data Fig. 10a for Trial III: ZH-161 and full results of in vivo Trials I and II including other PCY-hit NADs tested.* **g,** Trial IV: *in vivo* treatment of Vortioxetine (VORT; 10mg/kg) in combination with 1st- and 2nd-line glioblastoma chemotherapies; Temozolomide (TMZ; 50mg/kg) and Lomustine (CCNU; 20mg/kg) compared to single-agent treatments and negative vehicle control in ZH-161 tumor-bearing mice (n=5-6 mice per group). Combination treatments, TMZ+VORT/CCNU+VORT, both *P*=0.0007; Single-agents, TMZ/CCNU/VORT, all *P*=0.0018. **f-g,** Survival plotted as Kaplan–Meier curves and P values calculated using log-rank (Mantel-Cox) test. Censored mice denoted as tick marks. *P*-values: not significant (ns) $P > 0.05$, *$P < 0.05$, **$P < 0.01$, ***$P < 0.001$, ****$P < 0.0001$.

Extended Data Figure 1

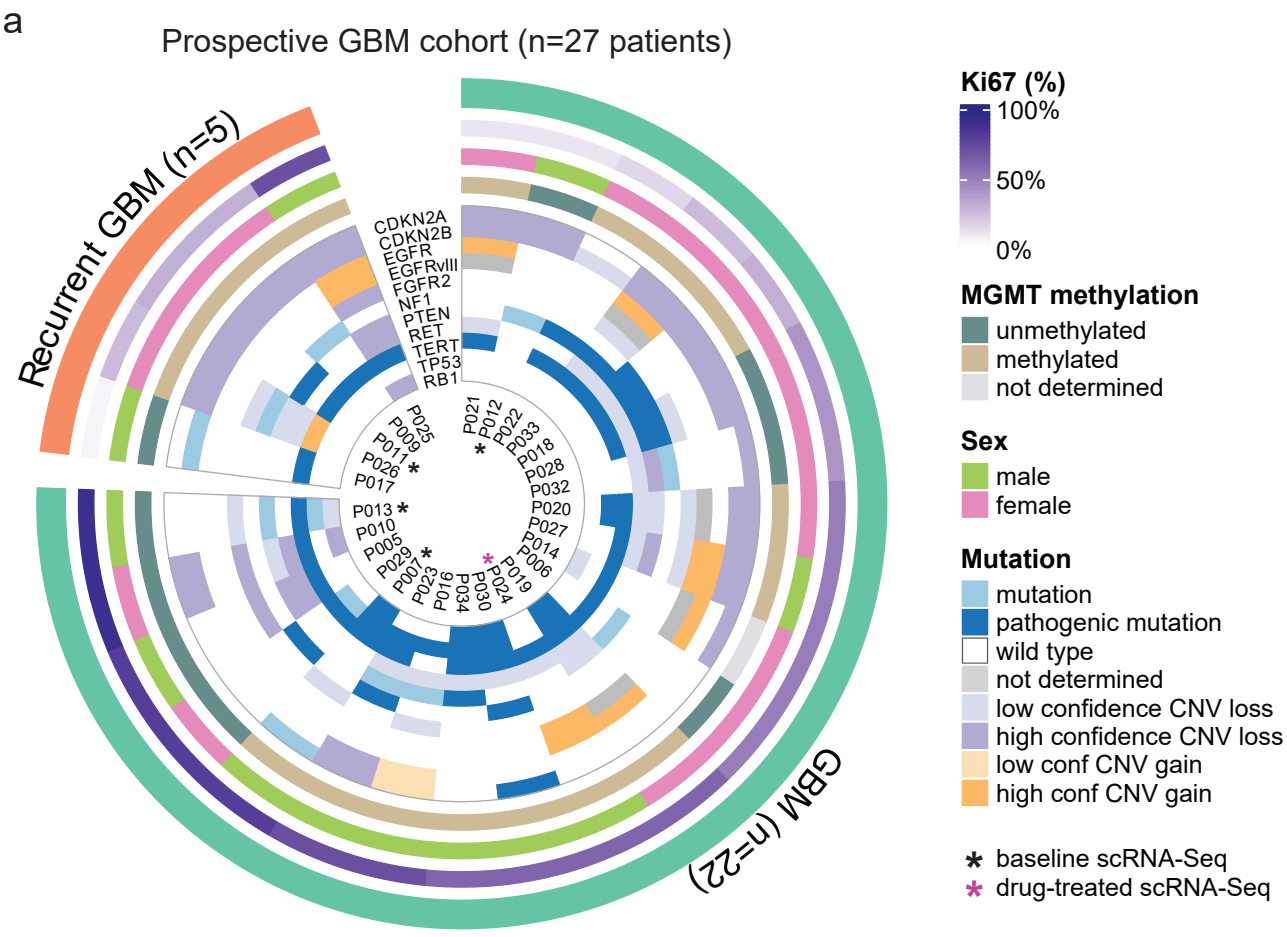

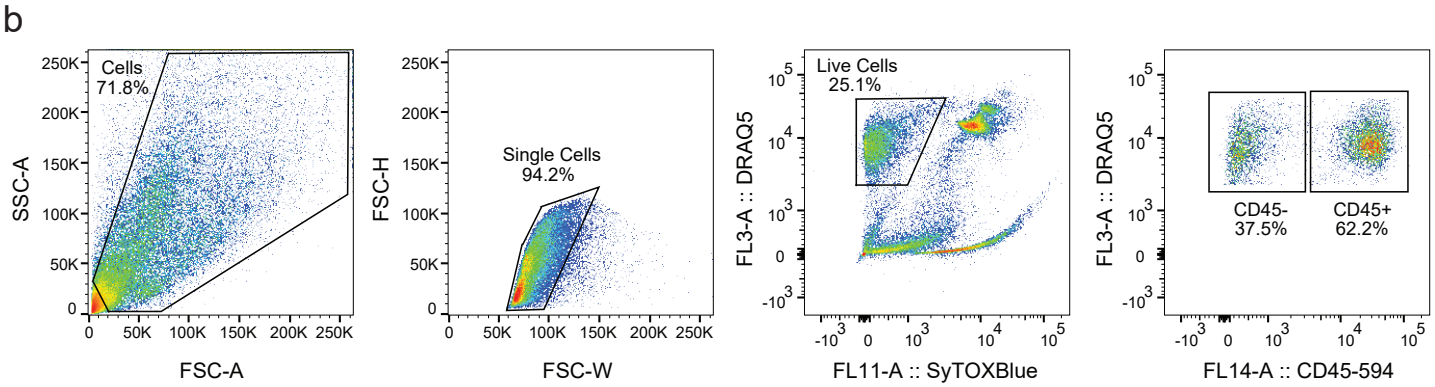

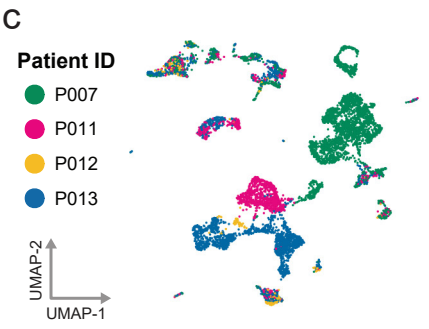

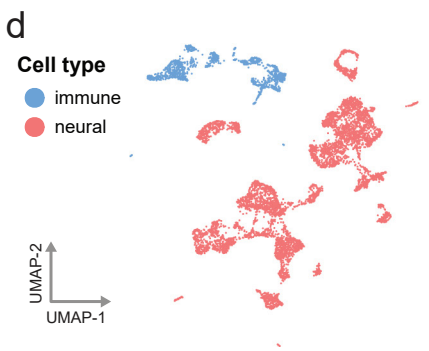

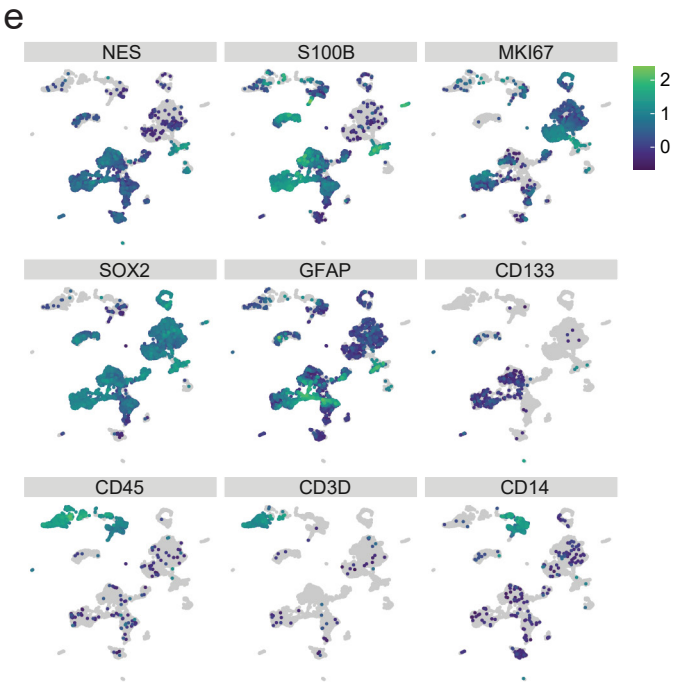

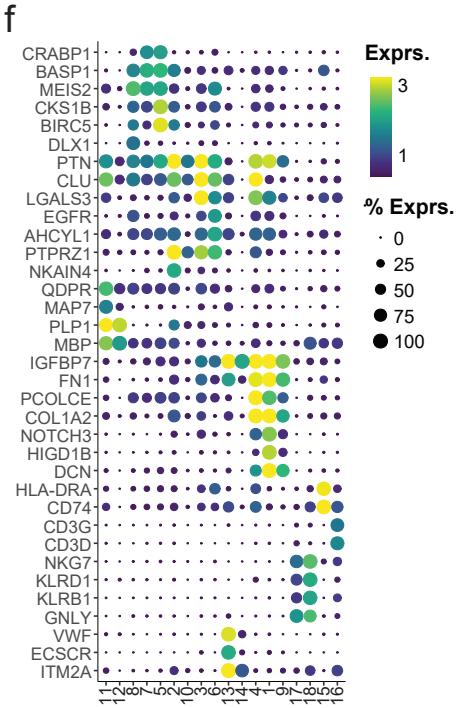

Extended Data Figure Legends

Extended Data Fig. 1: Glioblastoma prospective cohort overview and single-cell RNA-sequencing of four patient samples

a, Overview of the glioblastoma prospective patient cohort (n=27 patients) visualized as a circos plot. Concentric circles from outermost to innermost show primary versus recurrent tumor status, Ki67 labeling index, sex, *MGMT* promoter methylation status, and the most frequent genetic alterations (n=11) determined by targeted next-generation sequencing (NGS). Asterisks (*) denote patient samples for which scRNA-Seq was also performed (black, n=4 patients at baseline; pink, n=1 patient after drug treatment). CNV; copy number variation. *See Supplementary Table 1,2 for full cohort information*. **b**, Representative FACS gates of patient sample P011 to enrich for glioblastoma cells prior to scRNA-Seq (50,000 cells shown). Live viable cells were enriched by first gating DRAQ5+DAPI- cells, then sorting CD45+ and CD45- populations separately. **c**, UMAP projection of 7684 single-cell transcriptomes from four glioblastoma patient samples colored by patient (P007; 3475 cells, P011; 1490 cells, P012; 330 cells, P013; 2389 cells). **d**, UMAP projection of 7684 single-cell transcriptomes as in *Figure 1c* colored by cell type lineage. **e**, scRNA-Seq log10(expression) of key glioblastoma and immune marker genes. **f**, Top marker genes per scRNA-Seq cluster in *Figure 1c* that are expressed in more than 10 percent of cells in the respective cluster. Columns correspond to cluster ids and circle sizes scale with the percent of cells within each cluster expressing each gene. Color scale represents log10(mean+0.1) expression.

Extended Data Figure 2

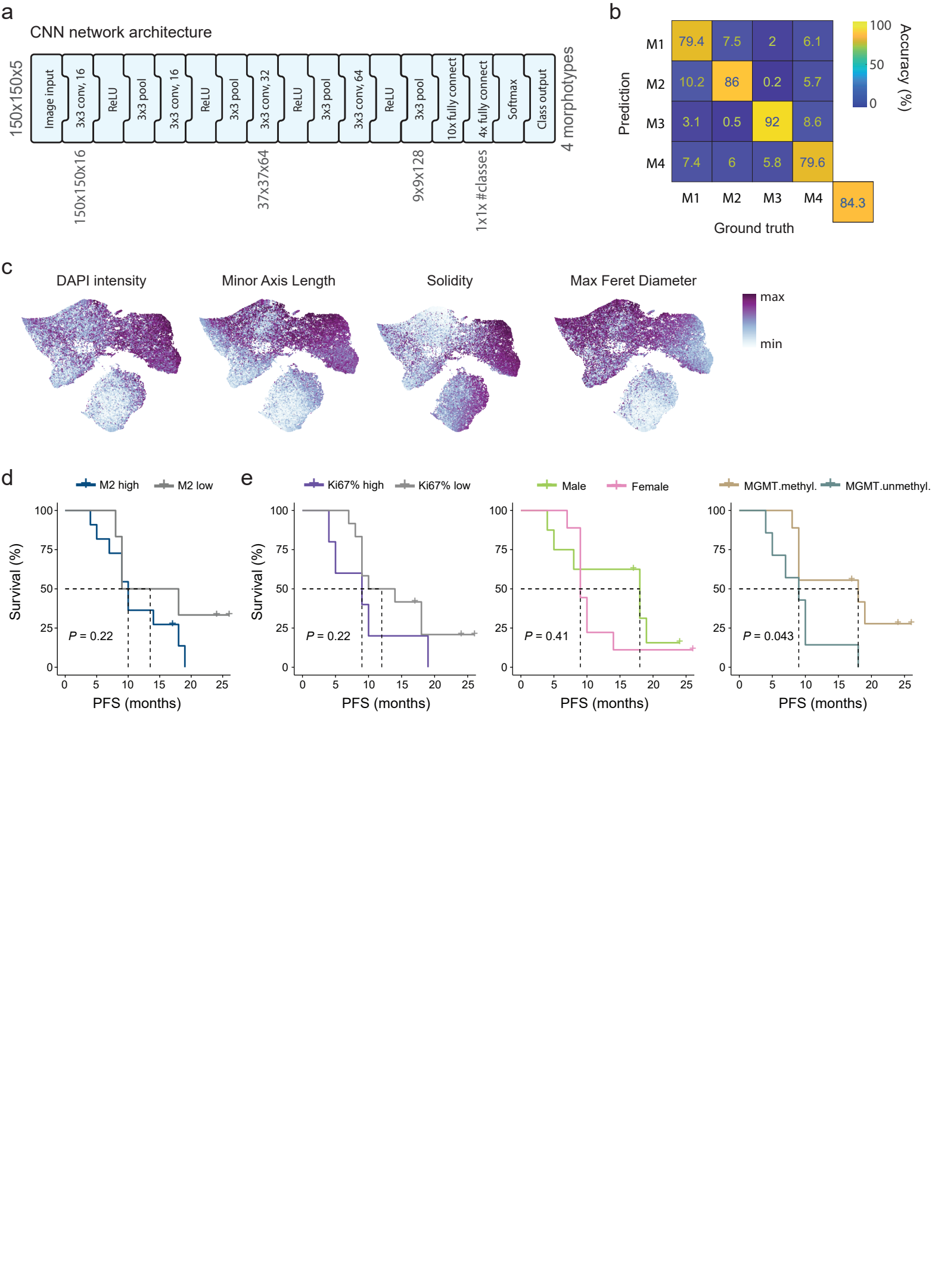

Extended Data Fig. 2: Deep learning of glioblastoma stem cell morphologies and clinical parameter-based stratification of patient survival

a, Architecture of the convolutional neural network (CNN) used to train the glioblastoma stem cell (GSC) morphologies, derived from a modified AlexNet [85]. **b,** Performance of the trained GSC morphology CNN in classifying the manually curated test image dataset consisting of Nestin+ single-cell crops (n=10,204 images) into the corresponding four GSC morphotypes (M1-M4). Accuracy of cell classification shown as a confusion matrix. **c,** UMAP projection of the morphological CNN feature space of 84,180 single cells (up to n=1000 cells per morphotype and patient, n=27 patients). CNN feature space consists of ten dimensional activations taken from the 2nd-last fully connected layer of the network. Cells are colored by the local median of selected single-cell features as in *Figure 1g*. **d,** Morphotype (M2) abundance-based stratification of progression-free survival (PFS) in primary glioblastoma patients (n=17 patients) plotted as Kaplan-Meier survival curves. M2-high; n=11, M2-low; n=6 patients; *P*=0.22 (ns). **e,** Clinical parameter-based stratification of progression-free survival (PFS) in primary glioblastoma patients (n=17 patients) plotted as Kaplan-Meier survival curves. From left to right, histopathological Ki67% labeling index, sex, and *MGMT* promoter methylation status (n=1 patient with undertermined MGMT status ommitted). **d-e,** For continuous parameters such as M2 morphotype abundance and Ki67%, the optimal cut-point for patient stratification (high, low) is determined by maximally selected rank statistics. Survival curves are compared using the log-rank (Mantel-Cox) test. Censored patients in the prospective cohort indicating ongoing responses (tick marks).

Extended Data Figure 3

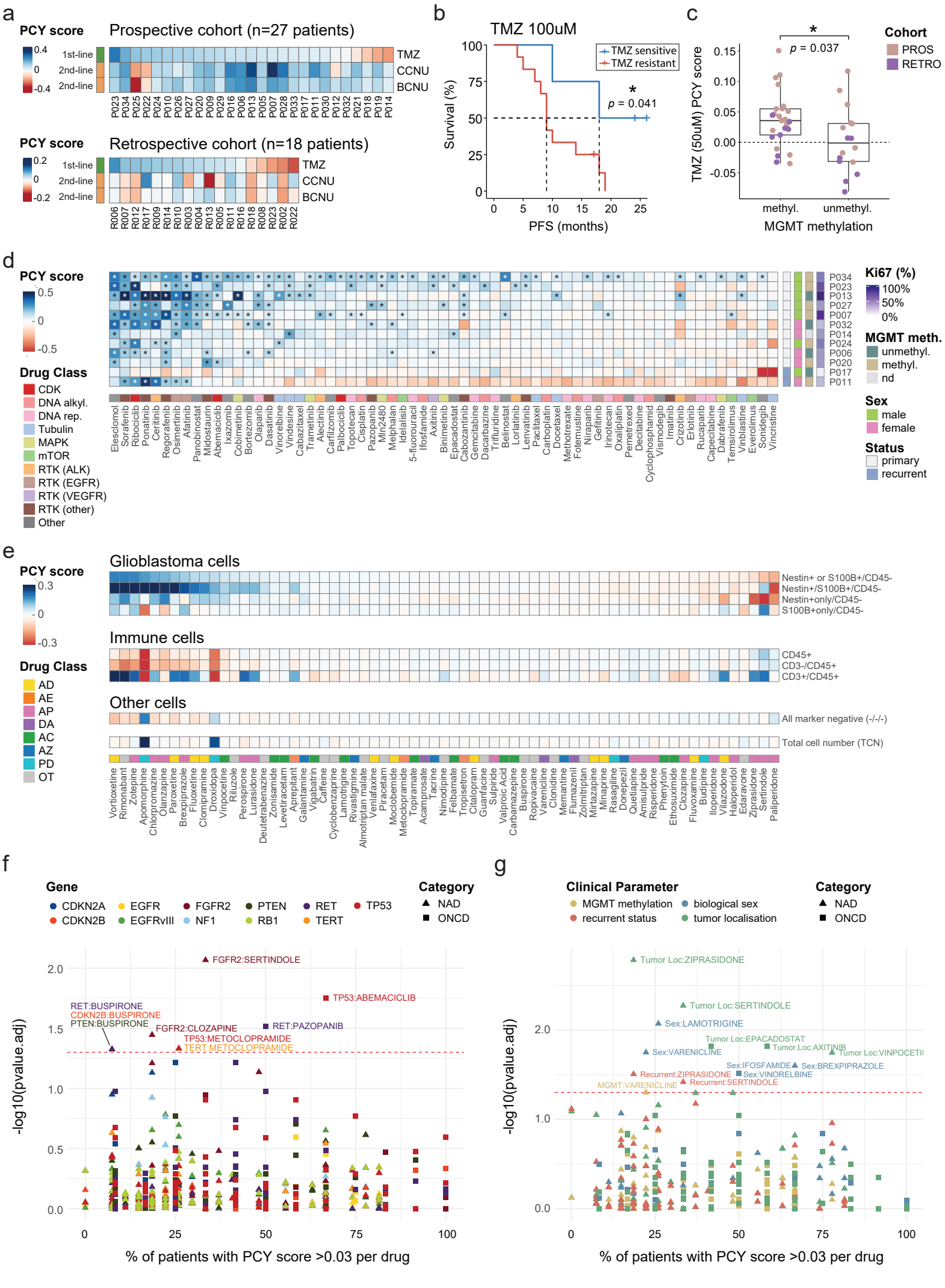

Extended Data Fig. 3: Patient *ex vivo* drug response relates to clinical parameters, tumor composition, and mutational profiles

a, Glioblastoma drug (GSDs; rows; n=3 drugs) response across glioblastoma patient samples (columns; prospective cohort, n=27 patients; retrospective cohort, n=18 patients). Glioblastoma drug response is averaged across four concentrations for Temozolomide (TMZ; 1st-line chemotherapy; 50, 100, 250, 500µM; annotated green) and Lomustine/Carmustine (Lomustine, CCNU; Carmustine, BCNU; 2nd-line chemotherapies; 10, 50, 100, 250µM; annotated orange). Heatmap color scale indicates the PCY score of Nestin+ or S100B+ cells. **b,** Temozolomide (100µM) *ex vivo* sensitivity-based stratification of progression-free survival (PFS) in the prospective glioblastoma cohort (n=16 patients; *P*=0.041) plotted as Kaplan-Meier curves. All patients received TMZ as 1st-line treatment in the clinic with censored patients in the prospective cohort indicating ongoing responses (tick marks). Survival curves are compared using the log-rank (Mantel-Cox) test and optimal cut-point for patient stratification determined by maximally selected rank statistics. **c,** Temozolomide (50µM) *ex vivo* response of glioblastoma patients (n=41 patients across both cohorts; y-axis) stratified by *MGMT* promoter methylation status. Only patients with an annotated *MGMT* status were included for this analysis. Unmethyl; unmethylated, Methyl; methylated. Wilcoxon rank sum test, *P*=0.037. Boxplots show 25th–75th percentiles with a line at the median; whiskers extend to 1.5 times the interquartile range. Dots indicate individual patient values colored by cohort. **d,** Drug response matrix of oncology drugs (ONCDs; columns; n=65 drugs) across glioblastoma patient samples (rows; n=12 patients). Heatmap color scale indicates the PCY score of glioblastoma cells (Nestin+ or S100B+). Annotations per patient sample (rows; right of heatmap) indicate the clinical parameters Ki67 labeling index, *MGMT* promoter methylation status (unmethyl; unmethylated, methyl; methylated, nd; not determined), Sex, and recurrent tumor status (Status). Annotation per drug (columns; underneath heatmap) indicates oncology drug class as in *Figure 2c*. Asterisks (*) denote FDR-adjusted $P < 0.05$. **e,** Drug response matrix of neuroactive drugs (NADs, n=67 drugs) averaged across glioblastoma patient samples (n=27 patients) for each cell population defined by immunofluorescence markers (Nestin, S100B, CD3, and CD45) and total cell number (TCN). Heatmap color scale indicates the mean PCY score of each respective population and drug classes are annotated as in *Figure 2c*. **f,** Pharmacogenomic analysis of the most common genetic alterations (n=11) in glioblastoma patients and *ex vivo* drug response. Each datapoint represents a [gene:drug] association, where x-axis denotes the percent of patients for which the respective drug's PCY score >0.03 and the y-axis denotes FDR-adjusted *P*-values for the association. **g,** As in **f**, but for associations between clinical parameters in glioblastoma patients and *ex vivo* drug response. Each datapoint represents a [clinical parameter:drug] association, where x-axis denotes the percent of patients for which the respective drug's PCY score >0.03 and the y-axis denotes FDR-adjusted *P*-values. **f,g** Colored by gene and shape denote drug category. Red dashed line indicates the significance threshold. Significant associations are annotated. *P*-values were calculated using the Wilcoxon rank sum test for two groups, and for three or more groups, the Kruskal-Wallis test was used. For ONCD associations, the following genetic mutations or clinical parameters had less than 3 patients in any category and were thus not analyzed: Genetic, *EGFRvIII*, *NF1*, *TERT*, *RB1*; Clinical, Recurrent status. **a,d,e,** Outliers beyond color scale limits were correspondingly set to minimum and maximum values. *P*-values: *P < 0.05.

Extended Data Figure 4

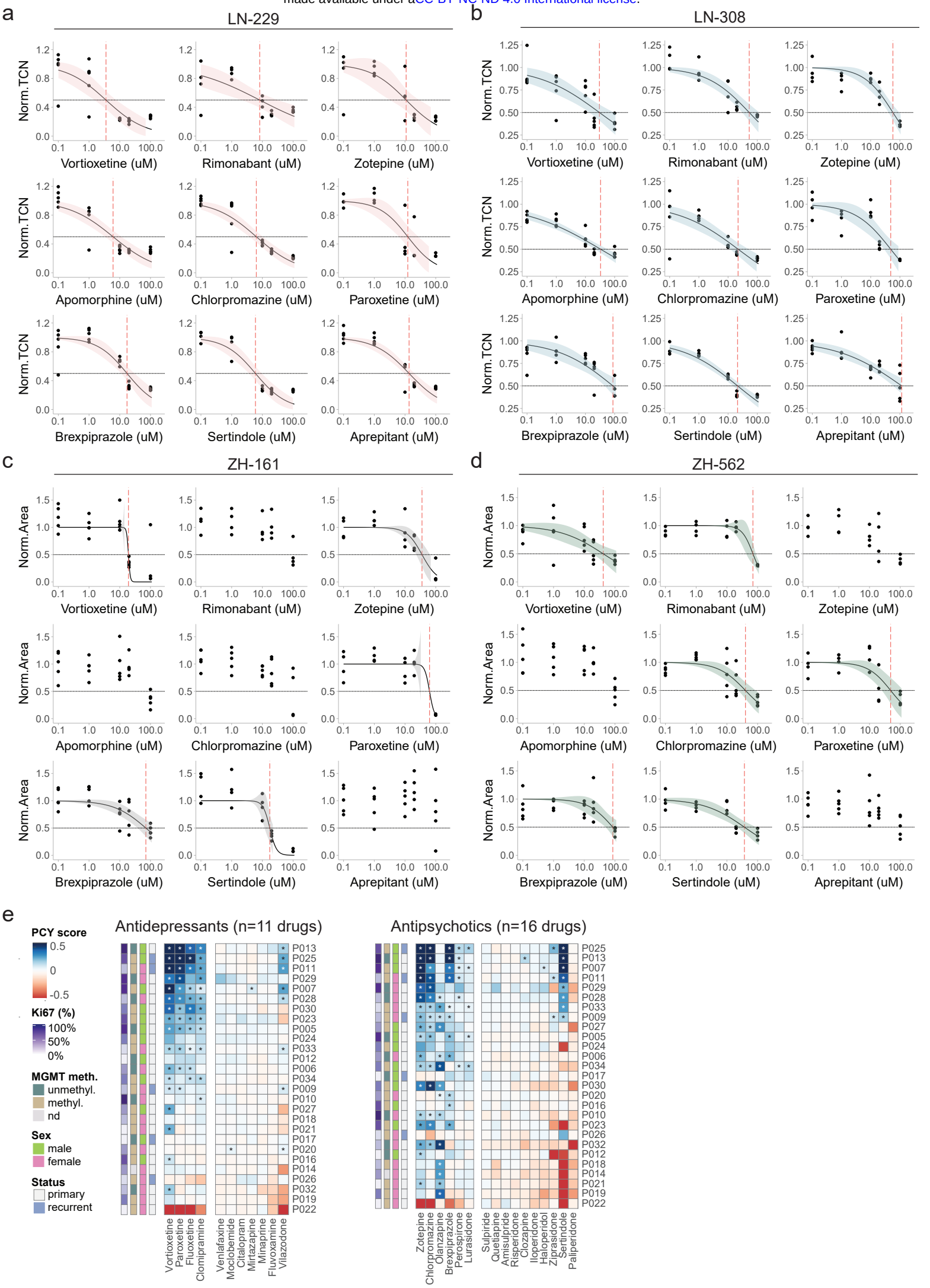

Extended Data Fig. 4: Dose-response to top neuroactive drugs across glioblastoma cell lines and patient *ex vivo* drug response to antidepressants and antipsychotics

a-d, Dose-response curves of glioblastoma cell lines (**a,** LN-229; **b,** LN-308; **c,** ZH-161; **d,** ZH-562) of a subset of top neuroactive drugs (n=9 drugs) across five different concentrations. X-axis represents logarithmically spaced drug concentrations while y-axis denotes for **a-b,** Relative cell count normalized to DMSO control and for **c-d,** Relative area of 2D-projected spheroids normalized to DMSO control. Individual well replicates are plotted as black dots (n=3-5 replicate wells/drug, n=15 DMSO wells). Dose-response curves (solid lines) are fitted when possible with a two-parameter log-logistic distribution with 95% confidence intervals (colored per cell line) and ED50 (red vertical dashed lines). **e,** Drug response matrix of antidepressants (left, n=11 drugs) and antipsychotics (right, n=16 drugs) across glioblastoma patient samples (n=27 patients) subsetted from the original matrix shown in *Figure 2b*. Color scale depicts the PCY score of glioblastoma cells (Nestin+ or S100B+). Outliers beyond color scale limits were correspondingly set to minimum and maximum values. Annotations per patient sample (rows; left of heatmap) indicate the clinical parameters Ki67 labeling index, MGMT promoter methylation status (unmethyl; unmethylated, methyl; methylated, nd; not determined), Sex, and recurrent tumor status (Status). Asterisks (*) denote FDR-adjusted $P < 0.05$.

Extended Data Figure 5

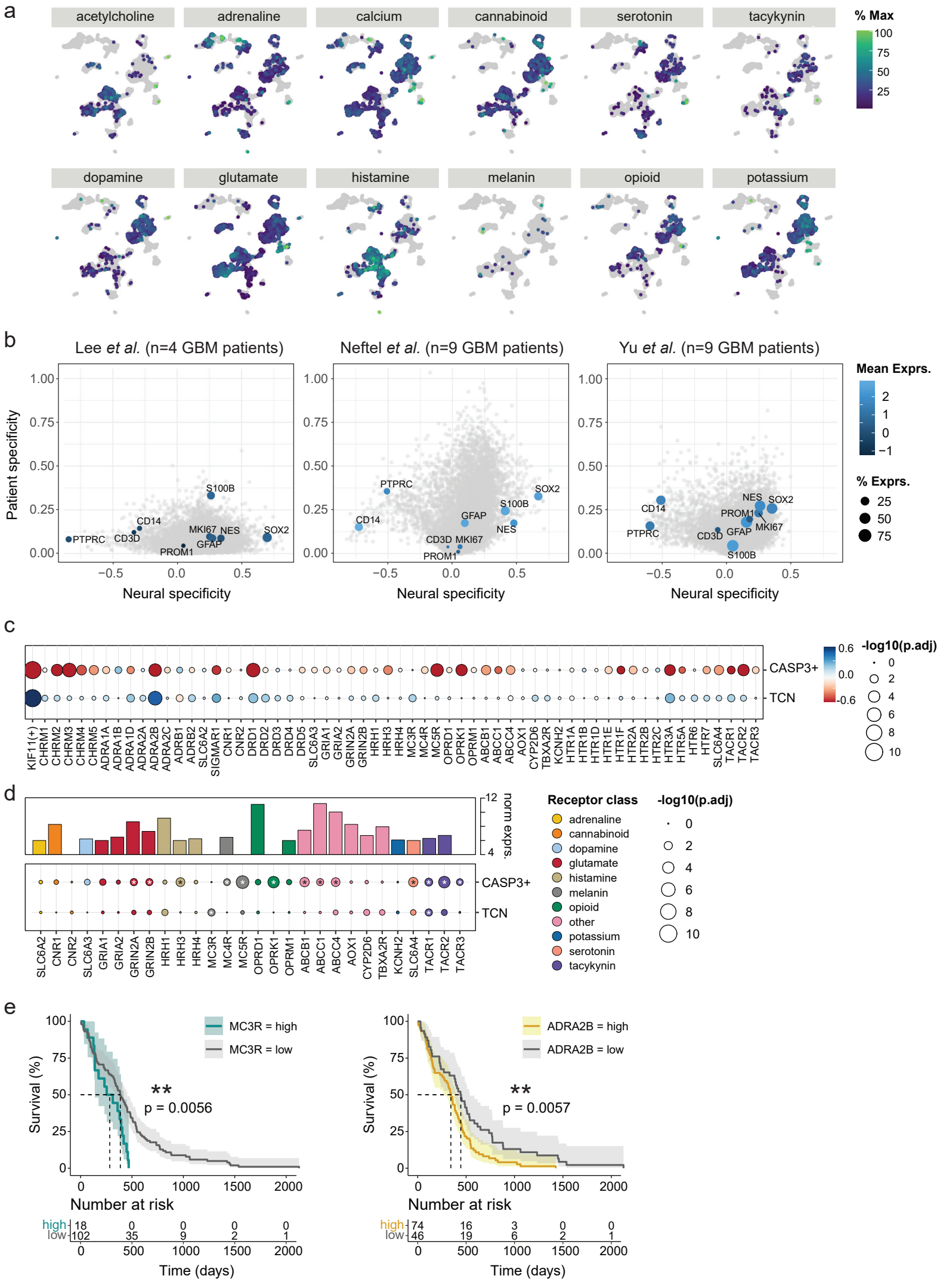

Extended Data Fig. 5: Single-cell heterogeneity and functional dependencies of primary neuroactive drug targets

a, UMAP projection of 7684 single-cell transcriptomes from four glioblastoma patient samples (P007, P011, P012, P013) as in *Figure 1c*, colored by aggregate scRNA-Seq expression across primary target genes (PTG) per receptor class in *Figure 3b*. Color scaled to percent of maximum expression per receptor class. **b**, Neural specificity score (x-axis) versus patient specificity score (y-axis) for three independent glioblastoma scRNA-Seq datasets. Each dot represents a gene, with key marker genes from *Extended Data Figure 1e* annotated with labels. Key marker gene color represents mean expression across cells in which the gene was detected and dot size scales with percent of expressed cells. All other genes detected in the respective datasets are colored in grey. (Lee *et al.*, *this study*; n=4 patients, n=7684 cells, n=15668 genes; Neftel *et al.*, n=9 patients, n=13519 cells, n=22160 genes; Yu *et al.*, n=9 patients, n=4307 cells, n=19098 genes; see *Methods* for further detail). **c-d**, siRNA-mediated gene silencing of PTGs in LN-229 cells. Total cell number reduction (TCN) and cleaved CASP3+ fraction increase (CASP3+) depicted as a circle per gene (columns). Circle sizes scale with the –log10(FDR-adjusted *P* value). **c,** Color represents the PCY score calculated using the FLUC siRNA condition as a negative (-) control reference including all tested PTGs corresponding to *Supplementary Table 5* (n=59 siRNA conditions). **d,** Color represents the receptor class of each PTG including PTGs not visualized in *Figure 3d* shown. Asterisks (*) denote FDR-adjusted $P < 0.05$. Adjacent bar plot represents baseline expression (DESeq2 vsd-normalized RNA-Seq counts) of each PTG in LN-229 cells. **e,** Survival analysis and associated risk tables of the TCGA primary glioblastoma cohort (n=120 patients) based on MC3R (left) and ADRA2B (right) expression measured by RNA-Seq. Optimal cut-point for patient stratification (high, low) is determined by maximally selected rank statistics. Survival curves are compared using the log-rank (Mantel-Cox) test. 95% confidence intervals are indicated in shaded curves.

Extended Data Figure 6

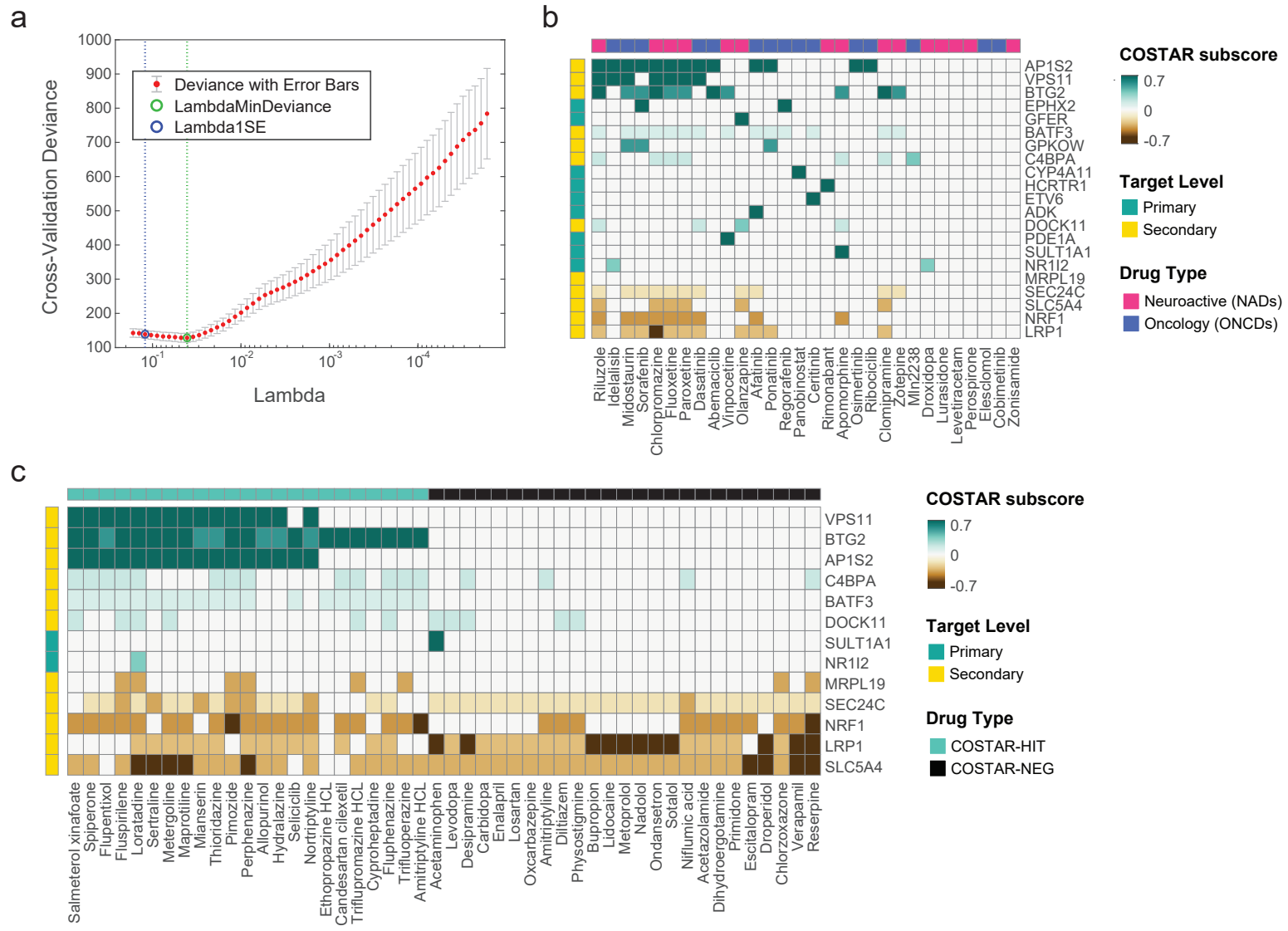

Extended Data Fig. 6: Convergence of secondary drug targets analyzed by regularized regression (COSTAR) identifies a drug-target connectivity signature predictive of anti-glioblastoma efficacy

a, Visualization of the local optimum in the cross-validated predictive power of COSTAR LASSO regression when fitting a binomial model to predict drug activity by PCY (hit vs neg) based on a drugs connectivity pattern (COSTAR constellation). X-axis denotes the Lambda regularization parameter and the y-axis denotes the goodness-of-fit indicating the cross-validated error of the model (deviance). Red dots and light grey error bars indicate the average and standard deviation in deviance across 20 bootstrapped runs. Vertical dashed lines and colored circles indicate either the Lambda value with the minimal mean squared error (green, MSE) or the more conservative Lambda value with minimal MSE plus one standard deviation (blue, MSE+1STD). **b**, Heatmap visualizing the COSTAR subscores of PCY-hit drugs that were part of the COSTAR training data (columns; n=30 drugs) to primary and secondary drug targets (rows). Drug type (NAD, ONCD) is annotated above. **c**, COSTAR subscores of COSTAR-predicted drugs that were chosen for experimental validation in glioblastoma patient samples (columns; n=23 COSTAR-HIT drugs; n=25 COSTAR-NEG drugs) to primary and secondary drug targets (rows). Drug type (COSTAR-HIT, COSTAR-NEG) is annotated above. **b-c,** Heatmap color scale indicates the COSTAR subscore which is the LASSO model coefficient multiplied by the integrated connectivity of drug to target mapping. Target genes with COSTAR LASSO coefficients >0.1 are displayed. Target level (primary or secondary target) is annotated per gene on the left.

Extended Data Figure 7

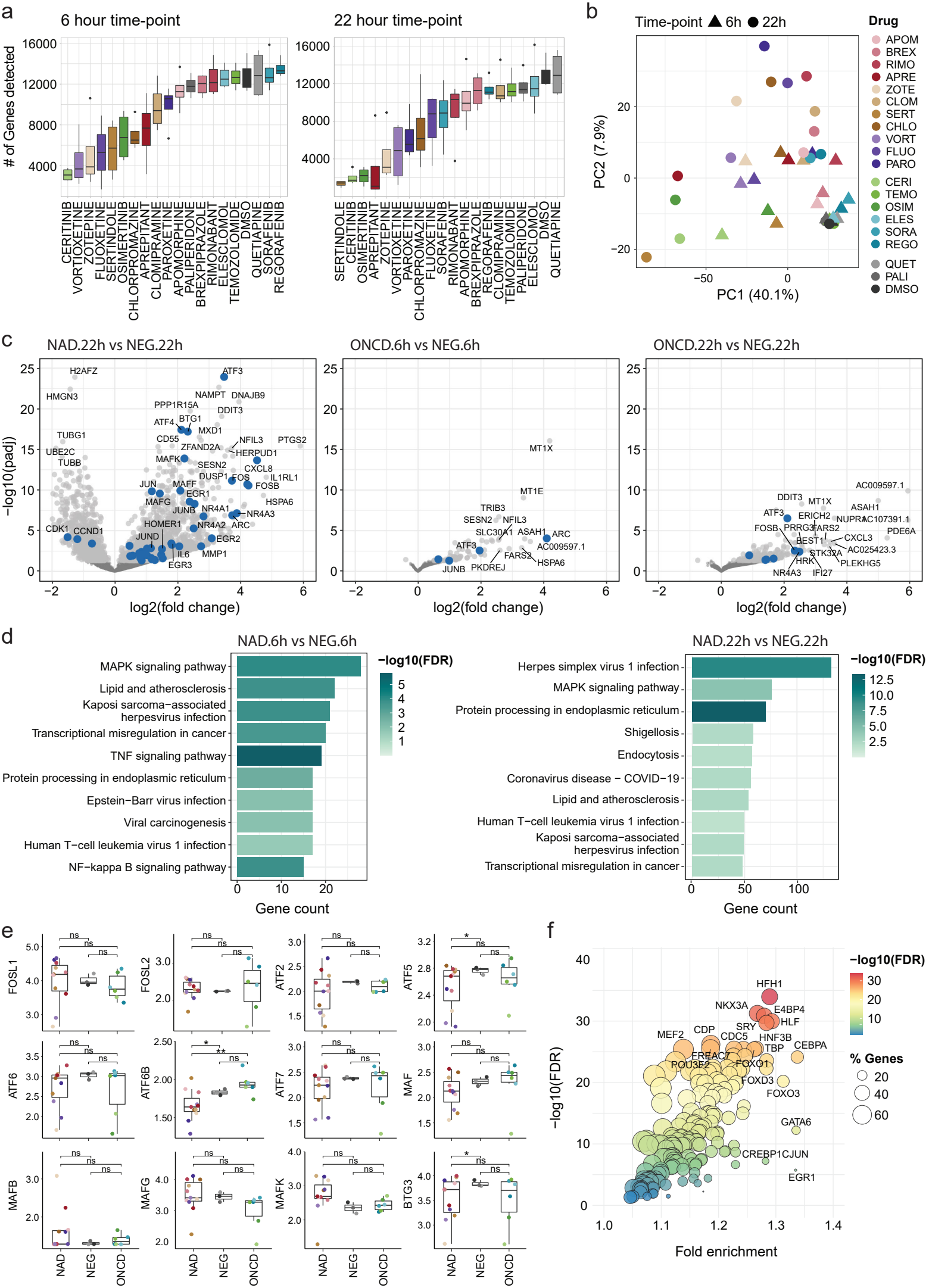

Extended Data Fig. 7: DRUG-Seq reveals a consistent transcriptional response to neuroactive drugs with anti-glioblastoma efficacy

a, Number of genes detected (y-axis) per drug condition (columns) and by time-point (left and right panel) in the DRUG-Seq data (n=20 drugs, n=2 time-points, n=4 replicates per drug/time-point). **b**, Principal component analysis (PCA) of averaged DESeq2 vsd-normalized RNA-Seq counts per drug. Points are colored by drug and shape indicates time-point. **c**, Comparisons of drug induced transcriptional profiles by DRUG-Seq shown as Volcano plots (log2(fold change) versus –log10(adjusted P-value)) for NADs vs NEGs (22h, left), ONCDs vs CTRLs (6h, middle), and ONCDs vs CTRLs (22h, right). Genes above a –log10(0.05 adjusted P-value) threshold plotted as light grey dots, and non-significant genes as dark grey dots. Highlighted genes (blue) include AP-1 transcription factor (TF) network genes (Pathway Interaction Database; PID AP1 PATHWAY; [84]) and key COSTAR signature genes. **d**, Top enriched KEGG terms for differentially expressed genes based on DESeq2 comparisons of NADs vs NEGs (6h, left) and NADs vs NEGs (22h, right). Bars represent the number of differentially expressed genes present in the annotation, and colors indicate –log10(false discovery rate). **e**, Expression of AP-1 transcription factor family and BTG genes additional to *Figure 4d*. Visualization and statistical tests as in *Figure 4d*. *P*-values: not significant (ns) $P > 0.05$, *$P < 0.05$, **$P < 0.01$ **f**, Transcription factor binding site enrichment analysis of genes that were upregulated in NAD treated cells in *Extended Data Figure 7c* (22h, left). Circles correspond to transcription factor annotations, circle sizes scale with the fraction of genes present in the annotation, and colors indicate –log10(false discovery rate). **a,e** Boxplots show 25th–75th percentiles with a line at the median; whiskers extend to 1.5 times the interquartile range.

Extended Data Figure 8

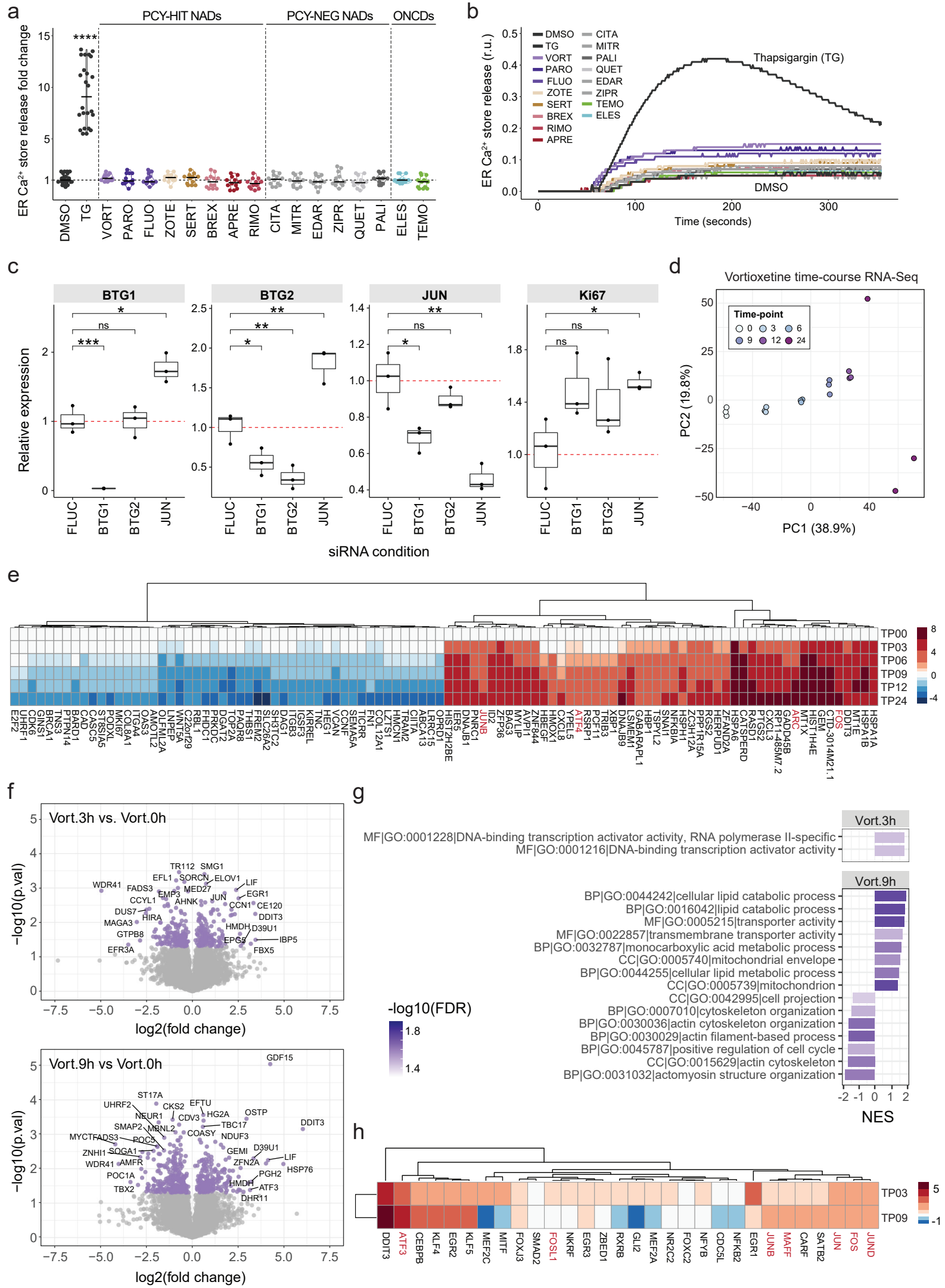

Extended Data Fig. 8: Measuring ER calcium store release, siRNA-mediated silencing of COSTAR signature genes, and Vortioxetine-induced transcriptomic and proteomic response

a, ER calcium store release upon drug treatment relative to DMSO vehicle control (fold change) measured by FLIPR assays in LN-229 cells (n=4 assay plates; n=18 conditions; n=12 wells/drug; DMSO and Thapsigargin, n=24 wells each). Thapsigargin (TG) was used as a positive control that induces ER calcium store depletion. Calcium levels for each condition were calculated by averaging calcium levels after drug treatment (190-430 seconds interval). Different drug categories including PCY-hit NADs, n=8 drugs; PCY-neg NADs, n=6 drugs; PCY-hit ONCDs, n=2 drugs; and TG were compared. Two-sided t-test against DMSO vehicle control. *P*-values adjusted for multiple comparisons by Holm correction. *P*-values: TG, 2.86e-16. ****P < 0.0001. Line indicates the median value. **b**, Representative traces of ER calcium store release following drug treatment corresponding to *Extended Data Figure 8a*. RFU; relative fluorescence units. **c**, Relative gene expression (y-axis) of BTG1, BTG2, JUN and Ki67 (panels) upon siRNA knockdown of FLUC, BTG1, BTG2, and JUN (columns) normalized to the FLUC negative control siRNA (n=3 biological replicates; black dots). Boxplots show 25th–75th percentiles with a line at the median; whiskers extend to 1.5 times the interquartile range. **d**, Principal component analysis (PCA) of averaged DESeq2 vsd-normalized RNA-Seq counts following Vortioxetine treatment (20µM) in LN-229 cells (n=3 replicates/time-point). Points are colored by time-point. **e**, Heatmap of log2(fold change) in gene expression per time-point (rows; relative to 0h) for the top 100 genes (columns) contributing to the first principal component (PC1) in *Extended Data Figure 8d*. TP; time-point. AP-1 transcription factors and AP-1 effector genes are labeled in red. **f**, Volcano plots of log2(fold change) versus –log10(*P*-value) corresponding to 3 hours versus 0 hours (top; Vort.3h vs. Vort.0h) and 9 hours versus 0 hours (bottom; Vort.9h vs. Vort.0h) comparisons of proteomics measurements following Vortioxetine treatment (Vort, 20µM; n=3 biological replicates/condition) in LN-229 cells. Plotted are proteins above a –log10(0.05 P-value) threshold (purple), and non-significant proteins (grey). Select gene names are shown. **g**, Gene Ontology (GO) gene set enrichment analysis of signed –log10(P-values) of both time-point comparisons from *Extended Data Figure 8f*. Bars represent the normalized enrichment score (NES) and colors indicate –log10(false discovery rate). **h**, Heatmap depicting log2(fold change) in protein expression per time-point (rows; relative to 0h) for the proteins (columns) contributing to enriched GO term “GO:0001216 DNA-binding transcription activator activity” in *Extended Data Figure 8g*. TP; time-point. AP-1 transcription factors are labeled in red.

Extended Data Figure 9

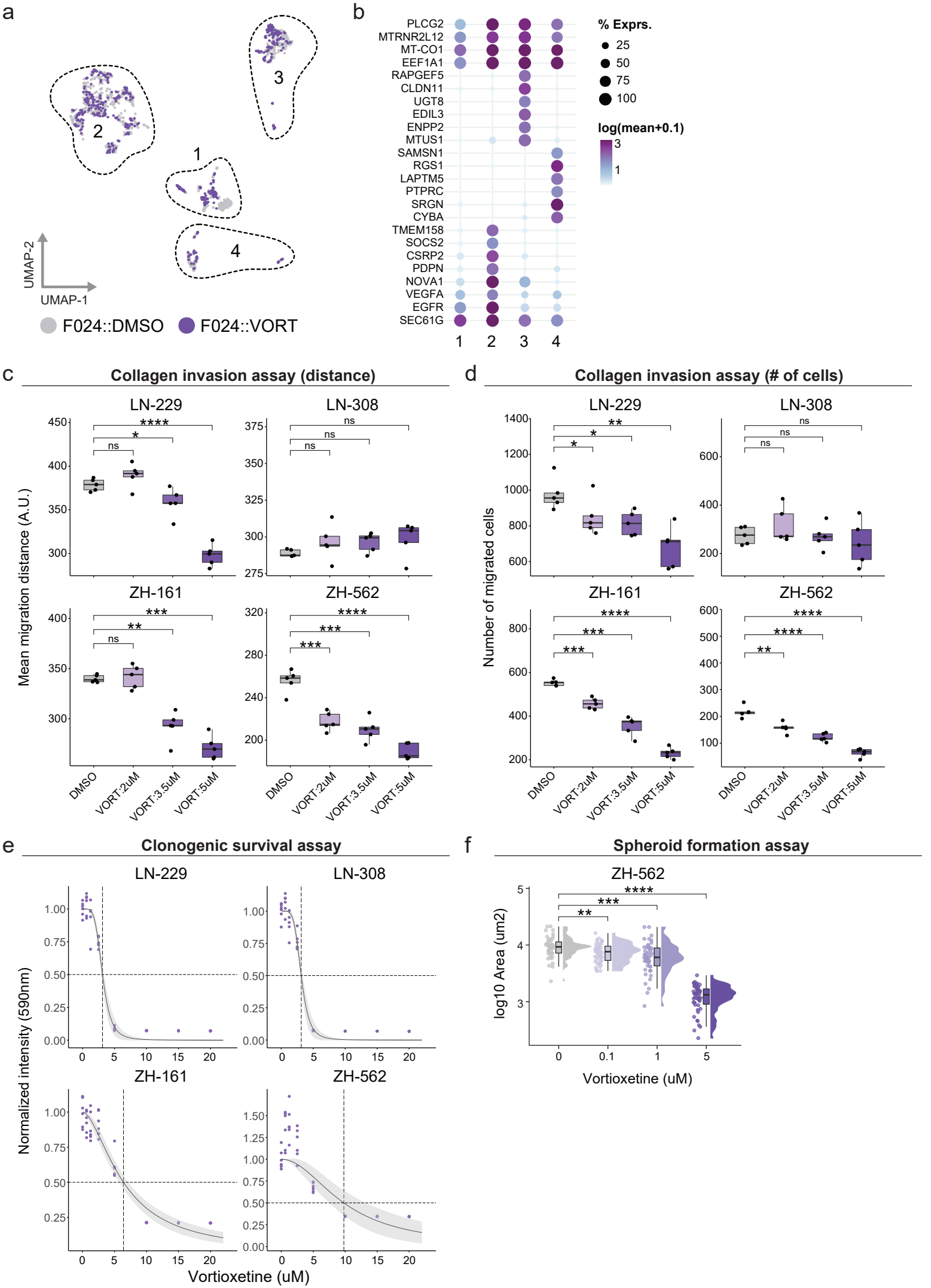

Extended Data Fig. 9: Single-cell RNA-sequencing of Vortioxetine-treated patient cells and the multi-faceted anti-glioblastoma effects of Vortioxetine

a, UMAP projection of 1736 single cells from glioblastoma patient sample P024 upon 3 hours of treatment with Vortioxetine (P024::VORT; n=577 cells; purple; 20µM) or DMSO vehicle control (P024::DMSO; n=1159 cells; grey). **b**, Expression levels of the top six marker genes per scRNA-Seq cluster in *Extended Data Figure 9a* that are expressed in more than 10% of cells in the respective cluster. Columns correspond to cluster ids and circle sizes scale with the percent of cells within each cluster expressing each gene. Color scale represents log10(mean+0.1) expression. **c,** Mean cell migration distance per condition (n=5 replicate wells) and **d,** number of migrated cells measured in a collagen-based spheroid invasion assay after 36 hours of Vortioxetine treatment (2, 3.5, 5µM) across four glioblastoma cell lines; LN-229 (n=560-1125 cells/well), LN-308 (n=137-426 cells/well), ZH-161 (n=200-574 cells/well), ZH-562 (n=38-253 cells/well). **e,** Clonogenic survival measured by a resazurin-based cell viability assay after 11-13 days of Vortioxetine treatment (7 concentrations; 0.625-20µM) across four glioblastoma cell lines; LN-229 LN-308, ZH-161, ZH-562. Cells were seeded in 96-well plates (50-500 cells/well) and normalized intensity (λEm = 590 nm) measured across six replicate wells/concentration. Dose-response fitted with a two-parameter log-logistic distribution with 95% confidence intervals (light grey) and ED50 (dashed lines). **g,** Spheroid formation analyzed by the 2D area of the ZH-562 line measured after 12 days of Vortioxetine treatment (0.1-5µM). Approximately 5 cells/well initially seeded in low-attachment U-bottom 384-well plates. DMSO; 0µM, n=45 replicate wells; 0.1µM, n=46, P=0.005; 1µM, n=47, P=0.00027; 5µM, n=46, P<0.0001. Data is shown per concentration as boxplot, individual data points, and histogram.

Extended Data Figure 10

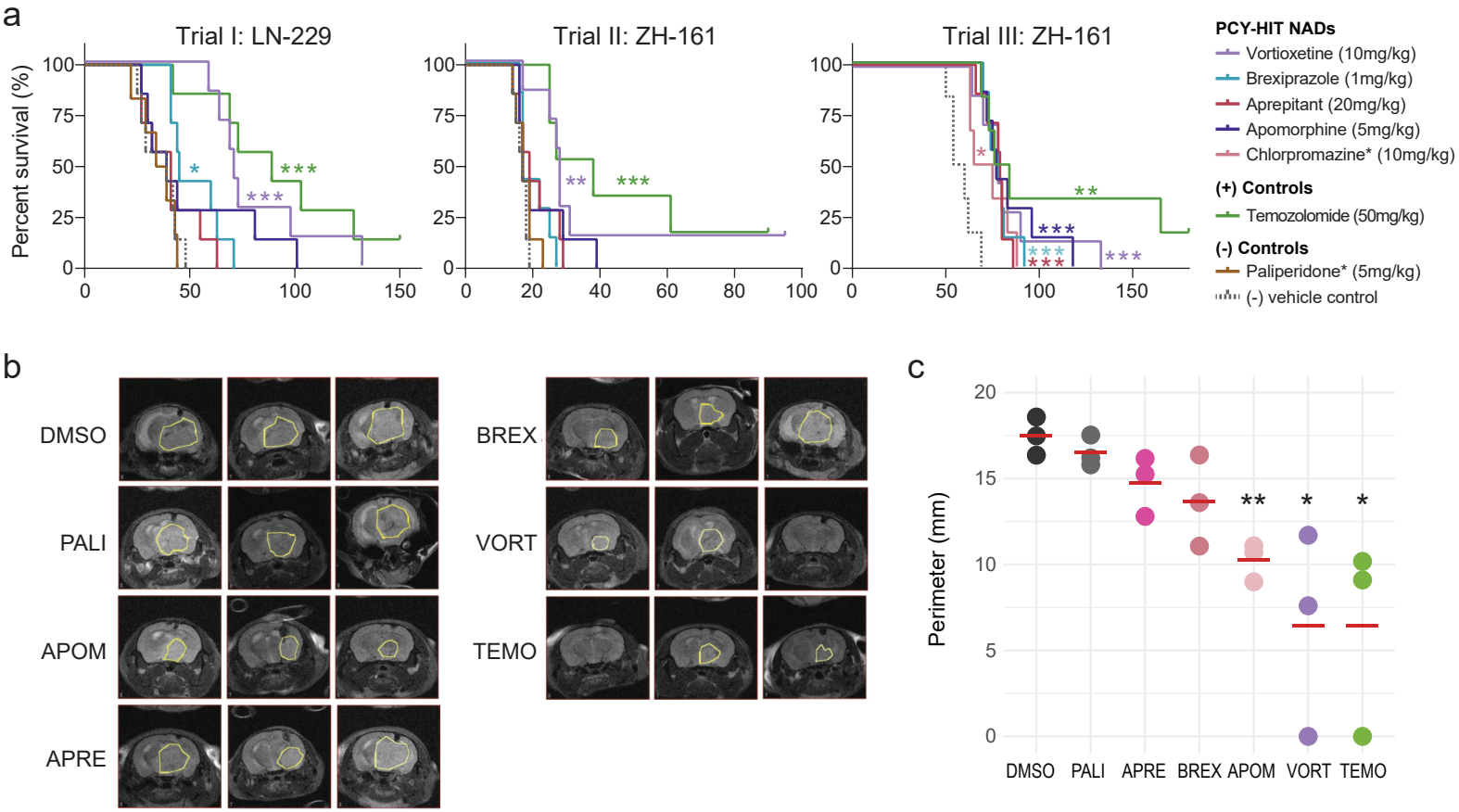

Extended Data Fig. 10: Top neuroactive drugs confer a significant survival benefit in orthotopic *in vivo* mouse models of glioblastoma

a, Complete survival analysis across three independent *in vivo* trials: Trial I: LN-229, Trial II: ZH-161, and Trial III: ZH-161, each with n=6-7 tumor-bearing mice per drug treatment group and n=7 drug treatments per trial. Mice were treated with their respective drugs for each trial intraperitoneally (*i.p.*) between days 5-21 after tumor implantation. PCY-HIT NADs: Vortioxetine (VORT; 10mg/kg; Trial I, *P*=0.0001; Trial II, *P*=0.0016; Trial III, *P*=0.0006); Brexpiprazole (BREX; 1mg/kg; Trial I, *P*=0.0249; Trial II, ns; Trial III, *P*=0.0002); Aprepitant(APRE; 20mg/kg; Trial I, ns; Trial II, ns; Trial III, *P*=0.0006); Apomorphine (APOM; 5mg/kg; Trial I, ns ; Trial II, ns; Trial III, *P*=0.0005); Chlorpromazine(CHLO; 10mg/kg; Trial III, *P*=0.011). Positive control (+): Temozolomide (TMZ; 50mg/kg; Trial I, *P*=0.0009 ; Trial II, *P*=0.0002; Trial III, *P*=0.0011). PCY-NEG NAD: Paliperidone (PALI; 5mg/kg; Trial I, ns; Trial II, ns), and a negative vehicle control. Drug names with asterisk (*) denote drugs used in a subset of the three *in vivo* trials. Survival plotted as Kaplan–Meier curves and *P*-values calculated using log-rank (Mantel-Cox) test. Censored mice denoted as tick marks. **b,** Representative MRI images of three ZH-161 transplanted mice (columns) after 15 days per drug treatment (n=7 drugs). Tumor perimeters are indicated in yellow. **c,** Quantification of tumor perimeters corresponding to *Extended Data Figure 10b*. Dots represent the perimeter in mm (y-axis) for individual mice per drug (columns), red lines indicate mean value. Two-sided t-test. *P*-values: Apomorphine (APOM; *P*=0.0014); Vortioxetine (VORT; *P*=0.034); Temozolomide (TMZ; *P*=0.0284). *P*-values: not significant (ns) P > 0.05, *P < 0.05, **P < 0.01, ***P < 0.001, ****P < 0.0001.

Methods

Patient sample processing and drug testing

Surgically removed tumors were collected at the University Hospital of Zurich (Universitätsspital Zürich, USZ) with approval by the Institutional Review Board, ethical approval number KEK-StV-Nr.19/08, BASEC number 2008-02002. Metadata of the prospective and retrospective glioblastoma patient cohorts including clinical parameters, experiment inclusion, and genetics summary can be found in *Supplementary Table 1*. The prospective cohort consists of patients where fresh tissue was taken directly after surgery (n=27 patients for drug screening, plus an additional n=3 patients for validation experiments). The retrospective cohort (n=18 patients) consists of patients for which snap-frozen bio-banked tissue was available covering a broad spectrum of progression-free survival. Retrospective samples were further selected based on quality control measures including cell viability, cell number, and the amount of debris present in the sample.

Tissue samples were first washed with PBS and cut into small pieces using single-use sterile scalpels. Subsequent dissociation was performed in reduced serum media (DMEM media; #41966029 with 2% FBS; #10270106, 1% Pen-strep; #15140122, and 25mM HEPES; #15630056, all products from Gibco) supplemented with Collagenase IV (1mg/ml) and DNaseI (0.1mg/ml) using the gentle MACS Octo Dissociator (Miltenyi Biotec, 130-096-427). Homogenates were filtered through a 70um Corning cell strainer (Sigma-Aldrich, CLS431751) and washed once with PBS containing 2mM EDTA. Myelin and debris removal was performed by a gradient centrifugation of the cell suspension in a 7:3 mix of PBS:Percoll (Sigma-Aldrich, P4937) and washed again with PBS. Dissociated patient cells were seeded at 0.5-1.5x10^4 cells/well into clear-bottom, tissue-culture treated, CellCarrier-384 Ultra Microplates (Perkin Elmer, #6057300). Prior to cell seeding, tested drugs were re-suspended as 5mM stock solutions and dispensed into the 384 well plates using an Echo 550 liquid handler (Labcyte) at their respective concentrations in a randomized plate layout to control for plate effects. Information regarding drugs used in this study can be found in *Supplementary Table 3*. For drug library testing (glioblastoma drugs, GSDs; neuroactive drugs, NADs; oncology drugs, ONCDs) cells were incubated in reduced serum media at 37°C, 5% CO_2 for 48 hours with drugs.

Targeted Next Generation Sequencing (NGS, Oncomine Comprehensive Assay v3)

Tissue blocks from patient-matched glioblastomas were used to determine genetic alterations including mutations, copy number variation and gene fusion. Formalin-fixed paraffin-embedded (FFPE) tissue blocks were collected from the Tissue Biobank at USZ archives. Tumor area was marked on the HE slide and relative tumor cell content was estimated by a trained pathologist. 1-3 cores cylinders (0.6 mm diameter) or 40 um from the tumor area of the FFPE blocks were used for DNA and RNA isolation. DNA was isolated with the Maxwell 16 FFPE Tissue LEV DNA Purification Kit (Promega, #AS1130) according to the manufacturer's recommendations. The double-strand DNA concentration (dsDNA) was determined using the fluorescence-based Qubit dsDNA HS Assay Kit. RNA was extracted with the Maxwell 16 FFPE Tissue LEV RNA Purification Kit (Promega, #AS1260) according to the manufacturer's recommendations. To avoid genomic DNA contamination, samples were pretreated with DNase1 for 15 min at room temperature (RT). Library preparation with 20 ng DNA or RNA input was conducted using the Oncomine Comprehensive Assay v3 following the manufacturer's instructions. Adaptor/barcode ligation, purification and equilibration was automated with Tecan Liquid Handler (EVO-100). NGS libraries were templated using Ion Chef and sequenced on a S5 (Thermo Fisher

Scientific), and data were analyzed using Ion Reporter Software 5.14 with Applied Filter Chain: Oncomine Variants (5.14) settings and Annotation Set :Oncomine Comprehensive Assay v3 Annotations v1.4.

For NGS data analysis, the Ion Reporter Software within Torrent Suite Software was used, enabling detection of small nucleic variants (SNVs), copy number variations (CNVs), gene fusions and indels from 161 unique cancer driver genes. Detected sequence variants were evaluated for their pathogenicity based on previous literature and the 'ClinVar' database [86]. Gene alterations described as benign or likely benign were not included in our results. Non-pathogenic mutations harboring a Minor Allele Frequency higher than 0.01 were not selected. The Default Fusion View parameter was selected. For CNV confidence range, the default filter was used to detect gains and losses using the confidence interval values of 5% confidence interval for Minimum Ploidy Gain over the expected value and 95% confidence interval for Minimum Ploidy Loss under the expected value. CNV low confidence range was defined for gain by copy number from 4 to 6 (lowest value observed for CNV confidence interval 5%:2.9) and loss from 0.5 to 1 (highest value observed for CNV confidence interval 95%:2.43). High confidence range was defined by gain up to 6 copy number (lowest value observed for CNV confidence interval 5%:4.54) and loss below 0.5 copy number (highest value observed for CNV confidence interval 95%:1.37). 5% and 95% interval confidence of all selected loss and gain are available in *Supplementary Table 2*. The minimum number of tiles required was eight. Results are reported as detected copy number.

Cell culture

The adherent human glioblastoma cell lines LN-229 (ATCC, #CRL-2611) and LN-308 were cultured in Dulbecco's modified Eagle medium (DMEM, #41966, Gibco) supplemented with 10% fetal bovine serum (FBS, #10270106, Gibco). LN-229 and LN-308 cells were passaged using Trypsin-EDTA (0.25%, Gibco, #25200056). For DRUG-seq, RNA-Seq, siRNA knockdown, and proteomics measurements using LN-229 cells, low-passage cells below passage 15 were used. The spheroid human glioblastoma-initiating cell lines ZH-161 and ZH-562 was generated from freshly isolated tumor tissue and cultured in Neurobasal medium (NB, #21103049, Gibco) supplemented with B27 (Gibco, #17504044), 20 ng/mL b-FGF (Peprotech, #AF-100-18B), 20 ng/mL EGF (Peprotech, #AF-100-15), 2 mM L-glutamine (Gibco, #25030081). ZH-161 and ZH-562 cells were passaged using Accutase (Stemcell Technologies, #07920). Cell lines were authenticated at the Leibniz Institute DSMZ (Braunschweig, Germany) and regularly tested negative for mycoplasma.

Immunocytochemistry

Cells were fixed with 4% PFA (Sigma-Aldrich, #F8775) in PBS and blocked in 5% FBS and 0.1% Triton containing PBS. For characterization of cellular composition across glioblastoma patient samples, cells were stained overnight at 4°C in blocking solution with the following antibodies and dilutions: Alexa Fluor® 488 anti-S100 beta (1:1000, Abcam, #ab196442, clone EP1576Y), PE anti-Nestin (1:150, Biolegend, #656806, clone 10C2), Alexa Fluor® 488 anti-CD3 (1:300, Biolegend, #300415, clone UCHT1), Alexa Fluor® 647 anti-CD45 (1:300, Biolegend, #368538, clone 2D1) and DAPI (1:1000, Biolegend, #422801, stock solution 10mg/ml). Due to the manufacturer discontinuation of the Alexa Fluor® 488 anti-S100 beta antibody, from patient sample P30 and onwards in the prospective cohort, samples were either stained with a self-conjugated Alexa Fluor® 488 anti-S100 beta antibody, where Alexa Fluor™ 488 NHS Ester (Thermo Scientific, #A20000) was conjugated to the anti-S100 beta antibody (Abcam, #ab215989, clone EP1576Y) or the following antibody combinations where the 488

and 555 channel markers were swapped: Alexa Fluor® 488 anti-Nestin (1:150, Biolegend, #656812, clone 10C2), Alexa Fluor® 555 anti-S100 beta (1:1000, Abcam, #ab274881, clone EP1576Y), PE anti-CD3 (1:300, Biolegend, #300441, clone UCHT1), Alexa Fluor® 647 anti-CD45 (1:300, Biolegend, #368538, clone 2D1).

Other antibodies used in this study include the following: Alexa Fluor® 647 anti-Tubulin Beta 3 (1:1000, Biolegend, #657406, clone AA10), Alexa Fluor® 555 anti-Cleaved Caspase-3 (1:500, Cell Signaling Technology, #9604S), Alexa Fluor® 546 anti-HOMER (1:300, Santa Cruz Biotechnology, #sc-17842 AF546, clone D-3), PE anti-CFOS (1:300, Cell Signaling Technology, #14609S, clone 9F6), FITC anti-ATF4 (1:300, Abcam, #ab225332), Alexa Fluor® 488 anti-JUND (1:300, Santa Cruz Biotechnology, #sc-271938 AF488, clone D-9), Alexa Fluor® 594 anti-CD45 (1:300, Biolegend, #368520, clone 2D1).

Confocal microscopy and image analysis

Imaging of the 384 well plates was performed with an Opera Phenix automated spinning-disk confocal microscope at 20x magnification unless otherwise specified (Perkin Elmer, HH14000000). Single cells were segmented based on their nuclei (DAPI channel) using CellProfiler 2.2.0. Downstream image analysis was performed with MATLAB R2019a-R2020a. Fractions of marker positive cells for each condition were derived for each patient sample based on the histograms of the local background corrected intensity measurements. Marker positive fractions were averaged across each well/condition and compared to the negative DMSO control.

Deep learning of glioblastoma stem cell morphologies

To generate a training dataset, Nestin+CD45- cells identified by immunofluorescence across the whole prospective glioblastoma patient cohort were cropped as 150x150 pixel images. These single-cell image crops were then manually-curated and labeled as four morphological classes (M1-M4 morphotypes) based on their shape, size, and presence of tumor microtubes. A convolution neural network (CNN) with a modified Alexnet architecture [85] as shown in *Extended Data Figure 2a* was then trained on this manually-curated training data with 12,757 images per class and 51,028 images in total. CNN training included usage of the Adam optimizer, with a mini-batch size of 150 and a maximum number of 30 epochs. The initial learning rate was set to 0.001 with a piecewise learning rate schedule and a drop factor of 0.01 every 6 epochs.

Network performance is shown as a confusion matrix in *Extended Data Figure 2b.* All Nestin+ single-cell images were subsequently classified by this pre-trained CNN to determine morphotype abundances across patients and drug conditions. For visualization of the CNN-based GSC morphotypes, UMAP plots were generated based on the CNN feature space that consists of ten dimensional activations taken from the 2nd-last fully connected layer of the network. The CNN feature space of 84,180 cells (maximally 1000 cells per class and patient, n=27 patients) was projected on the UMAP using the following parameters: distance metric, seuclidean; number of neighbors, 10; minimal distance, 0.06. Different morphological and marker-based features from the original cell segmentation determined by CellProfiler 2.2.0 such as cell area, eccentricity, and roundness, and mean marker intensity were selected for visualization.

siRNA knockdown and quantitative real-time PCR

All siRNAs used in the study were part of the MISSION® esiRNA (Sigma-Aldrich, Euphoria Biotech) library (*Supplementary Table 5*) and ordered as custom gene arrays (esiOPEN, esiFLEX). FLUC esiRNA

(EHUFLUC) targeting firefly Luciferase was used as a negative control, and KIF11 esiRNA (EHU019931) was used as a positive control for transfection and viability. For all siRNA experiments, low-passage LN-229 cells were used. siRNAs were transfected at 10ng/well in 384 well plates and 40ng/well in 96 well plates using Lipofectamine RNAiMAX (Invitrogen, #13778075). Imaging and drug incubation experiments were conducted in 384 well plates, while Incucyte live cell imaging and cell lysis preparation for RNA extraction and quantitative real-time PCR was performed in 96 well plates. For 384 well plates, both the siRNAs and Lipofectamine transfection reagent were dispensed using a Labcyte Echo liquid handler in a randomized plate layout to control for plate effects when possible. For data presented in *Figure 3d, Extended Data Figure 5c,d, and Extended Data Figure 8c,* cells were incubated at 37°C, 5% CO_2 for 48 hours following siRNA transfection before fixing, immunohistochemistry, and RNA extraction. For data presented in *Figure 4j*, following 48 hours of siRNA transfection, cells were incubated for an additional 24 hours with either DMSO vehicle control or Vortioxetine (10µM) before fixing and subsequent analysis.

siRNA knockdown efficiency and relative abundance for the following target genes; BTG1, BTG2, JUN, and MKI67 was measured by TaqMan™ Array plates (Applied Biosystems, Standard, 96-well Plate; Format 16 with candidate endogenous controls) using the TaqMan™ Fast Advanced Master Mix (Thermo Scientific, #A44360) on a QuantStudio™ 3 Real-Time PCR System (Applied Biosystems, #A28567). Total RNA from LN-229 cells was extracted using the Direct-zol RNA MicroPrep Kit (Zymo Research, #R2062), RNA concentration was measured using the Qubit 4 Fluorometer (Thermo Scientific), and cDNA synthesized with the iScript™ cDNA Synthesis Kit (Bio-Rad, #1708890). For each TaqMan biological replicate assay (n=3 replicates) 25ng of cDNA per sample was used. To calculate the relative abundance of each target gene, the geometric mean Ct value of four endogenous control genes (18s rRNA, GAPDH, HPRT, GUSB) was subtracted from each [sample-target gene] Ct value to derive the deltaCt (dCt) value. Then, the mean deltaCt value from FLUC negative control samples was subtracted from each [sample-target gene] deltaCt value to derive the delta-deltaCt (ddCt) value. Finally, relative abundance (fold-difference) of each [sample-target gene] was calculated as the 2^(-ddCt).

COSTAR: Convergence of secondary drug-targets analyzed by regularized regression

COSTAR is an interpretable molecular machine learning approach that utilizes logistic LASSO regression in a cross-validation setting to learn a multi-linear model that identifies the minimal set of drug-target connections that maximally discriminates PCY-hit drugs from PCY-negative drugs.

Drug-target connections were retrieved from the Drug Target Commons (DTC) [52]. DTC is a crowd-sourced platform that integrates drug-target bioactivities curated from both literature and public databases such as PubChem and ChEMBL. Drug-target annotations (DTC bioactivities) listed as of August 2020 were included, with the target organism limited to *Homo sapiens*. Among PCY-tested drugs in our NAD and ONCD libraries, 127 out of 132 drugs had DTC 'bioactivity' annotations. PTGs with biochemical associations to a given drug correspond to bioactivities with the inhibitory constant 'KI' as the 'End Point Standard Type'. Extended PTGs (ePTGs) include all annotated drug bioactivities. Secondary target genes (STGs) down-stream of ePTGs were retrieved by high-confidence protein-protein interactions annotated in the STRING database (interaction score≥0.6). The final drug-target connectivity map that was used for COSTAR consisted of 127 PCY-tested drugs, 975 extended primary targets, 10,573 secondary targets, and 114,517 network edges. The 127 drugs were labeled either as PCY-hits (n=30, equally split across NADs and ONCDs) or PCY-negative drugs (n=97) based on the ranked mean PCY score across patients.

A 20-fold cross-validated LASSO generalized linear model was trained in Matlab with the drug-target connectivity map as the predictor variable and PCY-hit status (hit vs. neg) as the binomially-distributed response variable to identify the optimal regularization coefficient (lambda) across a geometric sequence of 60 possible values. Final model coefficients were fitted using the lamba value corresponding to the minimum deviance in the cross-validation analysis shown in *Extended Data Figure 6a*. COSTAR performance was first evaluated on the training dataset, represented as a confusion matrix in *Figure 3g*. Using this trained linear model, COSTAR was next utilized as an *in silico* drug screening tool to predict the PCY-hit probability (COSTAR score) based on the connectivity of 1,120,823 compounds annotated in DTC (*Supplementary Table 6*). For interpretability, COSTAR subscores, defined as the individual connectivity to target genes multiplied by their respective coefficients (betas) in the linear model, can be investigated in *Extended Data Figure 6b,c*. COSTAR predictions from this *in silico* screen were further experimentally validated in glioblastoma patient samples on a set of new drugs predicted as either COSTAR-hits or COSTAR-negs (n=48 drugs total; n=23 COSTAR-hits; n=25 COSTAR-negs).

Single-cell RNA-Seq and analysis of other published datasets

Cryopreserved single-cell suspensions of glioblastoma patient samples that were part of the prospective cohort were thawed in reduced serum media (DMEM containing 2% FBS) and used for single-cell RNA-Seq experiments. Viability markers SYTOX Blue (1 µM, Thermo Fisher, #S11348) and DRAQ5 (1 µM, Biolegend, #424101) were added to the cell suspension at least 15 minutes before sorting. FACS gates were set based on CD45 (Alexa Fluor® 594 anti-CD45, 1:20, Biolegend, #368520, clone 2D1), SYTOX Blue and DRAQ5 intensities to isolate live CD45+ and CD45- populations as shown in *Extended Data Figure 1b* using the BD FACSAriaTM Fusion Cell Sorter. Cells were sorted into DNA LoBind® Eppendorf tubes (VWR, #525-0130), then CD45- cells were mixed with CD45+ cells at 2:1 to 10:1 ratios depending on cell availability to enrich for glioblastoma cells. For patient sample P024 that was used to measure the effect of Vortioxetine drug treatment, FAC-sorted cells were incubated for 3 hours with or without 20µM Vortioxetine before proceeding to library preparation. Single-cell RNA-Seq library preparation was performed using the Chromium Next GEM Single Cell 3' v3.0 and v3.1 kits (10x Genomics) according to the manufacturer's protocol. Libraries were sequenced on the Novaseq 6000 (Illumina). Read alignment to the GRCh38 human reference genome, generation of feature-barcode matrices, and aggregation of multiple samples were performed using the Cell Ranger analysis pipeline (10x genomics, versions 3.0.1 and 6.1.1). Four patient samples (P007, P011, P012, P013) were processed in November 2019 with the earlier version of 10x Genomics library prep kits and Cell Ranger analysis pipeline while the later sample (P024) was processed in September 2021. Quality control for this in-house dataset was performed by only analyzing high-quality cells with fewer than 10% of mitochondrial transcripts and genes that had at least a count of 2 in at least 3 cells.

To analyze additional glioblastoma patient samples by single-cell RNA-Seq, we utilized two published datasets: (Neftel et al. 2019) and (Yu et al. 2020). For Neftel *et al.*, we removed cells with less than 2^9 detected genes and/or more than 15% of mitochondrial transcripts. For Yu *et al.* the data was already prefiltered, but patient samples (7-9, 14-15) that did not correspond to glioblastoma (grade IV astrocytomas) were not included. For both datasets only genes that had at a count of 2 in at least 2 cells were included in the analysis.

Neural patient specificity scores and patient specificity scores for each gene were defined as follows: using the in-house dataset, we identified putative cell types by unsupervised clustering using Monocle [87] and annotated the clusters based on known marker genes as being either immune or neural cells.

We then obtained a list of differentially expressed genes between immune and neural cells using DESingle [88], using a logFC cutoff of 0.5. This yielded a list of 11571 neural-specific and 1157 immune specific genes. Using these lists as cell-type specific gene sets, we calculated an immune- and a neural score for each cell using singscore, and classified every cell in the additional datasets as either neural or immune based on a linear combination of both scores. To assess how specifically a gene is expressed in neural cells, we defined a '*neural specificity score'* as follows: [*neural specificity = fraction of neural cells expressing gene – fraction of immune cells expressing gene*] where we define expression of a gene in a cell as having any non-zero count. Thus, a positive score indicates that a gene is more often found in neural cells than in immune cells, and vice versa for negative scores. This score ranges from -1 (gene is expressed in all immune cells and no neural cells) to =1 (gene is expressed in all neural cells and no immune cells). Note that for low expressed genes, this score will be close to 0, reflecting the fact that we cannot make clear statements about cell type specificity for genes with expression values close to the detection limit of scRNA-Seq. To assess how much gene expression for a single gene varies across patients, we defined a '*patient specificity score'* as follows: First, for every gene *gi* and every patient *pj* we calculated a cell type composition independent fraction of cells expressing gene *gi* as [*Fraction_expressing_ij = fraction_expressing_immune_ij + fraction_expressing_neural_ij*]. We then defined patient specificity as the median absolute deviation (MAD) of fraction_expressing across all patients, thus defining [*Patient_specificity_i = mad(Fraction_expressing_i,:)*].

DRUG-Seq

High-throughput multiplexed RNA sequencing was performed with the Digital RNA with pertUrbation of Genes (DRUG-Seq) method as described in (Ye et al. 2018) with a few modifications. Modifications to the published method are the following: 1) extraction of RNA prior to cDNA reverse transcription with the Zymo Direct-zol-96 RNA isolation kit (Zymo, #R0256) 2) change of reverse transcription primers for compatibility with standard Illumina sequencing primers 3) cDNA clean-up prior to library amplification performed with the DNA Clean & Concentrator-5 kit (Zymo, #D4013) 3) tagmentation was performed with 2ng input and sequencing library generated using the Nextera XT library prep kit (Illumina, #FC-131-1024). In short, 1x10^4 LN-229 cells were plated in CellCarrier-96 Ultra Microplates (PerkinElmer, #6055302) and incubated overnight in reduced serum media at 37°C, 5% CO_2 prior to drug treatment. A total of 20 drugs (*Supplementary Table 3*) were profiled across two different time-points (6 hours and 22 hours; n=4 replicates per drug and time-point). These 20 drugs were selected to include PCY-hit NADs spanning diverse drug classes (n=11), PCY-hit ONCDs (n=7), PCY-negative NADs (n=2), and a DMSO control. Cells in drug-treated 96-wells were lysed with TRIzol™ Reagent (ThermoFisher, #15596018) and then subsequent cDNA and library prep was performed as described above. 100bp (80:20) paired-end reads were generated using Illumina's NextSeq 2000 platform.

Calcium assays on the FLIPR platform

For calcium assays, 24 hours prior to the experiment, LN-229 cells were seeded at a density of 70,000 cells/well on poly-D-Lysine-coated ViewPlateTM-96 F TC 96-well black polystyrene clear bottom microplates (PerkinElmer, #6005182) in 100µl full medium. Calcium 6 dye stock solution was prepared by dissolving a vial from Calcium 6 assay kit (Molecular Devices, #5024048) in 10 ml sterile-filtered nominal Ca^{2+} free (NCF), modified Krebs buffer containing 117mM NaCl, 4.8mM KCl, 1mM MgCl2, 5mM D-glucose, 10mM HEPES (pH 7.4) and 500µl aliquots were stored at -20°C. Before each experiment, the dye stock was freshly diluted 1:10 in NCF Krebs buffer and after removing the medium from the cells, 50µl of the diluted dye was applied per well. In order to allow the cells to absorb the dye into their cytosol, they were incubated at 37°C for 2 hours in the dark. The fluorescence Ca^{2+} measurements

were carried out using FLIPR Tetra® (Molecular Devices) where cells were excited using a 470–495nm LED module and the emitted fluorescence signal was filtered with a 515–575nm emission filter according to the manufacturer's guidelines.

In the ER Ca^{2+} store release assay, the stable baselines were established for 50 seconds before 50µl of 2µM (2X) Thapsigargin (Sigma-Aldrich, #T9033) or 40µM (2X) drug solutions freshly prepared in NCF Krebs buffer were robotically dispensed to the cells to determine whether the drugs impact the ER Ca^{2+} stores. Next, the cells were incubated and fluorescence was monitored in the presence of Thapsigargin or drugs for another 5 min. In the extracellular Ca^{2+} uptake assay, after initial recording of the baseline, 50µl of 4mM CaCl2 (2X) prepared in NCF Krebs buffer was dispensed onto the cells to re-establish a physiological 2mM calcium concentration and the fluorescence was monitored for 5 min. Next, 60µM (3X) drug solutions freshly prepared in Krebs buffer containing 2mM $CaCl_2$ were robotically dispensed to the cells and the fluorescence was recorded for an additional 4 min. The raw data was extracted with the ScreenWorks software version 3.2.0.14. The values represent average fluorescence level of the Calcium 6 dye measured over arbitrary selected and fixed time frames.

Time-course RNA-Seq library preparation and sequencing

Low passage LN-229 cells (passage 5-6) were seeded at 2x10^5 cells/well into in 6-well Nunc™ Cell-Culture Treated Multidishes (ThermoFisher, #140675) and incubated overnight in reduced serum media at 37°C, 5% CO_2 prior to drug treatment. The following day, Vortioxetine (Avachem Scientific, #3380) was manually added to each well at a final concentration of 20µM. At the start of the experiment, LN-229 cells that were not treated with Vortioxetine were collected as the 0 hour time-point. After 3, 6, 9, 12, and 24 hours following Vortioxetine treatment, drug-containing media was removed and cells were collected in TRIzol™ Reagent (ThermoFisher, #15596018). Total RNA was isolated using Direct-zol RNA MicroPrep Kit (Zymo Research, #R2062) according to the manufacturer's protocol and RNA quality and quantity was determined with the Agilent 4200 TapeStation. Sample RIN scores ranged from 5.9-10 (mean: 9.33). RNA input was normalized to 300-400 ng and RNA libraries were prepared using the Illumina Truseq stranded mRNA library prep following manufacturer's protocols. 100bp single-end reads were generated using Illumina's Novaseq 6000 platform with an average sequencing depth of approximately 50 million reads per replicate. Reads were mapped and aligned to the reference human genome assembly (GRCh38.p13) using STAR/2.7.8a and counts were extracted using featureCounts. Subsequent read normalization (variance stabilizing transformation, vsd-normalized counts) and RNA-Seq analysis including differential expression (DE) analysis was performed with the R package 'DESeq2' [89].

Time-course Proteomics

Cell preparation and Vortioxetine treatment was performed as in 'Time-course RNA-Seq library preparation' except cell numbers were scaled to be seeded in T-150 culture flasks and 3 time-points were measured (0, 3, 9 hours). Peptides for mass spectrometry measurements were prepared using the PreOmics iST kit (PreOmics) on the PreON (HSE AG). The robot was programmed to process 8 samples in parallel. During the first step of processing, cell pellets were resuspended in 50ul of lysis buffer and denatured for 10 minutes at 70°C. According to the manufacturer's protocol, this step was followed by 3 hours of digestion with trypsin and Lys-C. Peptides were dried in a speed-vac (Thermo Fisher Scientific) for 1 hour before being resuspended in LC- Load buffer at a concentration of 1 ug/ul with iRT peptides (Biognosys).

Samples were analyzed on an Orbitrap Lumos mass spectrometer (Thermo Fisher Scientific) equipped with an Easy-nLC 1200 (Thermo Fisher Scientific). Peptides were separated on an in-house packed 30 cm RP-HPLC column (Michrom BioResources, 75 µm i.d. x 30 cm; Magic C18 AQ 1.9 µm, 200 Å). Mobile phase A consisted of HPLC-grade water with 0.1% formic acid, and mobile phase B consisted of HPLC-grade ACN (80%) with HPLC-grade water and 0.1% (v/v) formic acid. Peptides were eluted at a flow rate of 250 nl/min using a non-linear gradient from 4% to 47% mobile phase B in 228 min. For data-independent acquisition (DIA), DIA-overlapping windows were used and a mass range of m/z 396-1005 was covered. The DIA isolation window size was set to 8 and 4 m/z, respectively, and a total of 75 or 152 DIA scan windows were recorded at a resolution of 30,000 with an AGC target value set to 1200%. HCD fragmentation was set to 30% normalized collision. Full MS were recorded at a resolution of 60,000 with an AGC target set to standard and the maximum injection time set to auto. DIA data were analyzed using Spectronaut v14 (Biognosys). MS1 values were used for the quantification process, peptide quantity was set to mean. Data were filtered using Qvalue sparse with a precursor and a protein Qvalue cut-off of 0.01 FDR. Interference correction and local cross-run normalization was performed. For PRM measurements, peptides were separated by reversed-phase chromatography on a 50 cm ES803 C18 column (Thermo Fisher Scientific) that was connected to a Easy-nLC 1200 (Thermo Fisher Scientific). Peptides were eluted at a constant flow rate of 200 nl/min with a 117 min non-linear gradient from 4–52% buffer B (80% ACN, 0.1% FA) and 25-50%B. Mass spectra were acquired in PRM mode on an Q Exactive HF-X Hybrid Quadrupole-Orbitrap MS system (Thermo Fisher Scientific). The MS1 mass range was 340–1,400 m/z at a resolution of 120,000. Spectra were acquired at 60,000 resolution (automatic gain control target value 2.0*10e5); Normalized HCD collision energy was set to 28%, maximum injection time to 118 ms. Monitored peptides were analyzed in Skyline v20 and results were uploaded to PanoramaWeb.

Incucyte live cell imaging

To measure cell proliferation in real-time, 2.5x10^3 LN-229 cells/well were plated in CellCarrier-96 Ultra Microplates (PerkinElmer, #6055302) 24 hours prior to the experiment, and transfected with BTG1, BTG2, and FLUC (-) MISSION® esiRNAs (Sigma-Aldrich, Euphoria Biotech, 40ng/well) using Lipofectamine RNAiMAX (Invitrogen, #13778075). Further details regarding siRNAs can be found in *Supplementary Table 5* and *Methods* related to 'siRNA knockdown and quantitative real-time PCR'**.** Real-time confluence of cell cultures (n=4 replicate wells/condition) was monitored by imaging every 2 hours for 7 days at 10x magnification with the 'phase' channel using the Incucyte live-cell analysis system S3 (Sartorius). Automatic image segmentation and analysis of the phase contrast images was performed by the Incucyte base analysis software (version 2020B).

Clonogenic survival assay

Adherent cells (LN-229: 50 cells; LN-308: 300 cells) were seeded in six replicates in 100 µL per well in 96-well plates and incubated overnight. On the following day, medium was replaced by fresh medium containing indicated final concentrations of Vortioxetine or DMSO. Glioblastoma-initiating cells (500 cells) were seeded in 75 µL medium and incubated overnight. Treatment was initiated by addition of 75 µL medium containing 2x concentrated Vortioxetine or DMSO to reach indicated final concentrations. DMSO concentration was kept at 0.5% for all treatments and controls. Following treatment addition, cells were cultured for 11 (LN-229) to 13 days (other cell lines) and clonogenic survival was estimated from a resazurin-based assay [90] using a Tecan M200 PRO plate reader (λEx = 560 nm / λEm = 590 nm).

Collagen-based spheroid invasion assay

Spheroid invasion assay was performed as described in (Kumar et al. 2015). Briefly, 2000 cells were seeded in six replicates into cell-repellent 96 U-bottom well plates (Greiner, #650979) and incubated for 48 hours to allow spheroid formation. Subsequently, 70 µL medium were removed, spheroids were overlaid with 70 µL 2.5% Collagen IV (Advanced Biomatrix, #5005-B) in 1xDMEM containing sodium bicarbonate (Sigma-Aldrich #S8761) and collagen was solidified in the incubator for 2 hours. Collagen-embedded spheroids were then overlaid with 100 µL chemoattractant (NIH-3T3-conditioned medium) containing 2x concentrated Vortioxetine/DMSO (0.5% final DMSO concentration across conditions) and incubated for 36 hours. Spheroids were stained with Hoechst and images were acquired on a MuviCyte imaging system (Perkin Elmer, #HH40000000) using a 4x objective. Images were contrast-enhanced and converted to binary using ImageJ/Fiji and quantified with the automated Spheroid Dissemination/Invasion counter software (aSDIcs), which quantifies the migration distance from the center of the spheroid for each detected cell nucleus [91].

In vivo drug testing

All animal experiments were done under the guidelines of the Swiss federal law on animal protection and were approved by the cantonal veterinary office (ZH98/2018). CD1 female nu/nu mice (Janvier, Le Genest-Saint-Isle, France) of 6 to 12 weeks of age were used in all experiments and 100’000 LN-229-derived- or 150’000 ZH-161-derived cells were implanted [92]. Tumor-bearing mice were treated from day 5 – day 21 after tumor implantation with intraperitoneally (*i.p.*) administered Vortioxetine daily 10mg/kg, Paliperidone daily 5mg/kg, Apomorphine daily 5mg/kg, Aprepitant daily 20mg/kg, Brexpiprazole daily 1mg/kg, Chlorpromazine three time per week 10mg/kg, Temozolomide 50mg/kg for five consecutive days, CCNU 20mg/kg at day 7 and 14 after tumor implantation, or daily DMSO control. Magnetic resonance imaging (MRI) was performed with a 4.7 T imager (Bruker Biospin, Ettlingen, Germany) when the first mouse became symptomatic. Coronal T2-weighted images were acquired using Paravision 6.0 (Bruker BioSpin).

References

1. Ostrom, Q. T., Cioffi, G., Waite, K., Kruchko, C. & Barnholtz-Sloan, J. S. CBTRUS Statistical Report: Primary Brain and Other Central Nervous System Tumors Diagnosed in the United States in 2014-2018. *Neuro. Oncol.* **23**, iii1–iii105 (2021).
2. Osswald, M. *et al.* Brain tumour cells interconnect to a functional and resistant network. *Nature* **528**, 93–98 (2015).
3. Venkatesh, H. S. *et al.* Neuronal Activity Promotes Glioma Growth through Neuroligin-3 Secretion. *Cell* **161**, 803–816 (2015).
4. Weil, S. *et al.* Tumor microtubes convey resistance to surgical lesions and chemotherapy in gliomas. *Neuro. Oncol.* **19**, 1316–1326 (2017).
5. Venkataramani, V. *et al.* Glutamatergic synaptic input to glioma cells drives brain tumour progression. *Nature* **573**, 532–538 (2019).
6. Venkatesh, H. S. *et al.* Electrical and synaptic integration of glioma into neural circuits. *Nature* **573**, 539–545 (2019).
7. Alcantara Llaguno, S. *et al.* Cell-of-origin susceptibility to glioblastoma formation declines with neural lineage restriction. *Nat. Neurosci.* **22**, 545–555 (2019).
8. Venkataramani, V. *et al.* Glioblastoma hijacks neuronal mechanisms for brain invasion. *Cell* **185**, 2899–2917.e31 (2022).
9. Cancer Genome Atlas Research Network. Comprehensive genomic characterization defines human glioblastoma genes and core pathways. *Nature* **455**, 1061–1068 (2008).
10. Brennan, C. W. *et al.* The somatic genomic landscape of glioblastoma. *Cell* **155**, 462–477 (2013).
11. Suvà, M. L. *et al.* Reconstructing and reprogramming the tumor-propagating potential of glioblastoma stem-like cells. *Cell* **157**, 580–594 (2014).
12. Neftel, C. *et al.* An Integrative Model of Cellular States, Plasticity, and Genetics for Glioblastoma. *Cell* **178**, 835–849.e21 (2019).
13. Varn, F. S. *et al.* Glioma progression is shaped by genetic evolution and microenvironment interactions. *Cell* **185**, 2184–2199.e16 (2022).
14. Stupp, R. *et al.* Radiotherapy plus concomitant and adjuvant temozolomide for glioblastoma. *N. Engl. J. Med.* **352**, 987–996 (2005).
15. Hegi, M. E. *et al.* MGMT gene silencing and benefit from temozolomide in glioblastoma. *N. Engl. J. Med.* **352**, 997–1003 (2005).
16. Weller, M. *et al.* EANO guidelines on the diagnosis and treatment of diffuse gliomas of adulthood. *Nat. Rev. Clin. Oncol.* **18**, 170–186 (2021).
17. Singh, S. K. *et al.* Identification of human brain tumour initiating cells. *Nature* **432**, 396–401 (2004).
18. Bao, S. *et al.* Glioma stem cells promote radioresistance by preferential activation of the DNA damage response. *Nature* **444**, 756–760 (2006).
19. Chen, J. *et al.* A restricted cell population propagates glioblastoma growth after chemotherapy. *Nature* **488**, 522–526 (2012).
20. Harder, B. G. *et al.* Developments in blood-brain barrier penetrance and drug repurposing for improved treatment of glioblastoma. *Front. Oncol.* **8**, 462 (2018).
21. Le Rhun, E. *et al.* Molecular targeted therapy of glioblastoma. *Cancer Treat. Rev.* **80**, 101896 (2019).
22. Gómez-Oliva, R. *et al.* Evolution of Experimental Models in the Study of Glioblastoma: Toward

Finding Efficient Treatments. *Front. Oncol.* **10**, 614295 (2020).
23. Patel, A. P. *et al.* Single-cell RNA-seq highlights intratumoral heterogeneity in primary glioblastoma. *Science* **344**, 1396–1401 (2014).
24. John Lin, C.-C. *et al.* Identification of diverse astrocyte populations and their malignant analogs. *Nat. Neurosci.* **20**, 396–405 (2017).
25. Lan, X. *et al.* Fate mapping of human glioblastoma reveals an invariant stem cell hierarchy. *Nature* **549**, 227–232 (2017).
26. Lee, J. H. *et al.* Human glioblastoma arises from subventricular zone cells with low-level driver mutations. *Nature* **560**, 243–247 (2018).
27. Couturier, C. P. *et al.* Single-cell RNA-seq reveals that glioblastoma recapitulates a normal neurodevelopmental hierarchy. *Nat. Commun.* **11**, 3406 (2020).
28. Yu, K. *et al.* Surveying brain tumor heterogeneity by single-cell RNA-sequencing of multi-sector biopsies. *Natl Sci Rev* **7**, 1306–1318 (2020).
29. Dolma, S. *et al.* Inhibition of Dopamine Receptor D4 Impedes Autophagic Flux, Proliferation, and Survival of Glioblastoma Stem Cells. *Cancer Cell* **29**, 859–873 (2016).
30. Caragher, S. P. *et al.* Activation of Dopamine Receptor 2 Prompts Transcriptomic and Metabolic Plasticity in Glioblastoma. *J. Neurosci.* **39**, 1982–1993 (2019).
31. Bi, J. *et al.* Targeting glioblastoma signaling and metabolism with a re-purposed brain-penetrant drug. *Cell Rep.* **37**, 109957 (2021).
32. Snijder, B. *et al.* Image-based ex-vivo drug screening for patients with aggressive haematological malignancies: interim results from a single-arm, open-label, pilot study. *Lancet Haematol* **4**, e595–e606 (2017).
33. Kornauth, C. *et al.* Functional Precision Medicine Provides Clinical Benefit in Advanced Aggressive Hematologic Cancers and Identifies Exceptional Responders. *Cancer Discov.* **12**, 372–387 (2022).
34. Heinemann, T. *et al.* Deep morphology learning enhances ex vivo drug profiling-based precision medicine. *Blood Cancer Discov* (2022) doi:10.1158/2643-3230.BCD-21-0219.
35. Malta, T. M. *et al.* Machine Learning Identifies Stemness Features Associated with Oncogenic Dedifferentiation. *Cell* **173**, 338–354.e15 (2018).
36. Dahlstrand, J., Collins, V. P. & Lendahl, U. Expression of the Class VI Intermediate Filament Nestin in Human Central Nervous System Tumors1. *Cancer Res.* **52**, 5334–5341 (1992).
37. Yuan, X. *et al.* Isolation of cancer stem cells from adult glioblastoma multiforme. *Oncogene* **23**, 9392–9400 (2004).
38. Zhang, M. *et al.* Nestin and CD133: valuable stem cell-specific markers for determining clinical outcome of glioma patients. *J. Exp. Clin. Cancer Res.* **27**, 85 (2008).
39. Vladimer, G. I. *et al.* Global survey of the immunomodulatory potential of common drugs. *Nat. Chem. Biol.* **13**, 681–690 (2017).
40. Conde, J. *et al.* Allosteric Antagonist Modulation of TRPV2 by Piperlongumine Impairs Glioblastoma Progression. *ACS Cent Sci* **7**, 868–881 (2021).
41. Severin, Y. *et al.* Multiplexed high-throughput immune cell imaging reveals molecular health-associated phenotypes. *bioRxiv* 2021.12.03.471105 (2021) doi:10.1101/2021.12.03.471105.
42. Shilts, J. *et al.* A physical wiring diagram for the human immune system. *Nature* (2022) doi:10.1038/s41586-022-05028-x.
43. Kirshner, J. R. *et al.* Elesclomol induces cancer cell apoptosis through oxidative stress. *Mol. Cancer Ther.* **7**, 2319–2327 (2008).
44. Guthrie, L. M. *et al.* Elesclomol alleviates Menkes pathology and mortality by escorting Cu to

cuproenzymes in mice. *Science* **368**, 620–625 (2020).
45. Xie, Q. *et al.* Mitochondrial control by DRP1 in brain tumor initiating cells. *Nat. Neurosci.* **18**, 501–510 (2015).
46. Bonnay, F. *et al.* Oxidative Metabolism Drives Immortalization of Neural Stem Cells during Tumorigenesis. *Cell* **182**, 1490–1507.e19 (2020).
47. Garofano, L. *et al.* Pathway-based classification of glioblastoma uncovers a mitochondrial subtype with therapeutic vulnerabilities. *Nat Cancer* **2**, 141–156 (2021).
48. Lombardi, G. *et al.* Regorafenib compared with lomustine in patients with relapsed glioblastoma (REGOMA): a multicentre, open-label, randomised, controlled, phase 2 trial. *Lancet Oncol.* **20**, 110–119 (2019).
49. Wick, W. *et al.* Phase II Study of Radiotherapy and Temsirolimus versus Radiochemotherapy with Temozolomide in Patients with Newly Diagnosed Glioblastoma without MGMT Promoter Hypermethylation (EORTC 26082). *Clin. Cancer Res.* **22**, 4797–4806 (2016).
50. Chinnaiyan, P. *et al.* A randomized phase II study of everolimus in combination with chemoradiation in newly diagnosed glioblastoma: results of NRG Oncology RTOG 0913. *Neuro. Oncol.* **20**, 666–673 (2018).
51. Babak, S. & Mason, W. P. mTOR inhibition in glioblastoma: requiem for a dream? *Neuro-oncology* vol. 20 584–585 (2018).
52. Tang, J. *et al.* Drug Target Commons: A Community Effort to Build a Consensus Knowledge Base for Drug-Target Interactions. *Cell Chem Biol* **25**, 224–229.e2 (2018).
53. Sheng, M. & Greenberg, M. E. The regulation and function of c-fos and other immediate early genes in the nervous system. *Neuron* **4**, 477–485 (1990).
54. Yap, E.-L. & Greenberg, M. E. Activity-Regulated Transcription: Bridging the Gap between Neural Activity and Behavior. *Neuron* **100**, 330–348 (2018).
55. Ye, C. *et al.* DRUG-seq for miniaturized high-throughput transcriptome profiling in drug discovery. *Nat. Commun.* **9**, 4307 (2018).
56. Li, J. *et al.* DRUG-seq Provides Unbiased Biological Activity Readouts for Neuroscience Drug Discovery. *ACS Chem. Biol.* **17**, 1401–1414 (2022).
57. Rouault, J. P. *et al.* Identification of BTG2, an antiproliferative p53-dependent component of the DNA damage cellular response pathway. *Nat. Genet.* **14**, 482–486 (1996).
58. Yuniati, L., Scheijen, B., van der Meer, L. T. & van Leeuwen, F. N. Tumor suppressors BTG1 and BTG2: Beyond growth control. *J. Cell. Physiol.* **234**, 5379–5389 (2019).
59. Eferl, R. & Wagner, E. F. AP-1: a double-edged sword in tumorigenesis. *Nat. Rev. Cancer* **3**, 859–868 (2003).
60. Karin, M., Liu, Z. g. & Zandi, E. AP-1 function and regulation. *Curr. Opin. Cell Biol.* **9**, 240–246 (1997).
61. Sanyal, S., Sandstrom, D. J., Hoeffer, C. A. & Ramaswami, M. AP-1 functions upstream of CREB to control synaptic plasticity in Drosophila. *Nature* **416**, 870–874 (2002).
62. Carlsson, P. & Mahlapuu, M. Forkhead Transcription Factors: Key Players in Development and Metabolism. *Dev. Biol.* **250**, 1–23 (2002).
63. Ho, K. K., Myatt, S. S. & Lam, E. W.-F. Many forks in the path: cycling with FoxO. *Oncogene* **27**, 2300–2311 (2008).
64. Benayoun, B. A., Caburet, S. & Veitia, R. A. Forkhead transcription factors: key players in health and disease. *Trends Genet.* **27**, 224–232 (2011).
65. Sheng, M., Thompson, M. A. & Greenberg, M. E. CREB: a Ca(2+)-regulated transcription factor phosphorylated by calmodulin-dependent kinases. *Science* **252**, 1427–1430 (1991).

66. Whitmarsh, A. J. & Davis, R. J. Transcription factor AP-1 regulation by mitogen-activated protein kinase signal transduction pathways. *J. Mol. Med.* **74**, 589–607 (1996).
67. Park, C. Y. *et al.* Tissue-aware data integration approach for the inference of pathway interactions in metazoan organisms. *Bioinformatics* **31**, 1093–1101 (2015).
68. Grünblatt, E., Mandel, S., Berkuzki, T. & Youdim, M. B. Apomorphine protects against MPTP-induced neurotoxicity in mice. *Mov. Disord.* **14**, 612–618 (1999).
69. Guilloux, J.-P. *et al.* Antidepressant and anxiolytic potential of the multimodal antidepressant vortioxetine (Lu AA21004) assessed by behavioural and neurogenesis outcomes in mice. *Neuropharmacology* **73**, 147–159 (2013).
70. Maeda, K. *et al.* Brexpiprazole I: in vitro and in vivo characterization of a novel serotonin-dopamine activity modulator. *J. Pharmacol. Exp. Ther.* **350**, 589–604 (2014).
71. Berger, M. *et al.* Hepatoblastoma cells express truncated neurokinin-1 receptor and can be growth inhibited by aprepitant in vitro and in vivo. *J. Hepatol.* **60**, 985–994 (2014).
72. Oliva, C. R., Zhang, W., Langford, C., Suto, M. J. & Griguer, C. E. Repositioning chlorpromazine for treating chemoresistant glioma through the inhibition of cytochrome c oxidase bearing the COX4-1 regulatory subunit. *Oncotarget* **8**, 37568–37583 (2017).
73. Torrisi, S. A. *et al.* Fluoxetine and Vortioxetine Reverse Depressive-Like Phenotype and Memory Deficits Induced by Aβ1-42 Oligomers in Mice: A Key Role of Transforming Growth Factor-β1. *Front. Pharmacol.* **10**, 693 (2019).
74. Lee, J.-K., Nam, D.-H. & Lee, J. Repurposing antipsychotics as glioblastoma therapeutics: Potentials and challenges. *Oncol. Lett.* **11**, 1281–1286 (2016).
75. Tan, S. K. *et al.* Drug Repositioning in Glioblastoma: A Pathway Perspective. *Front. Pharmacol.* **9**, 218 (2018).
76. Caragher, S. P., Hall, R. R., Ahsan, R. & Ahmed, A. U. Monoamines in glioblastoma: complex biology with therapeutic potential. *Neuro. Oncol.* **20**, 1014–1025 (2018).
77. Lee, J.-K. *et al.* Spatiotemporal genomic architecture informs precision oncology in glioblastoma. *Nat. Genet.* **49**, 594–599 (2017).
78. Lee, J.-K. *et al.* Pharmacogenomic landscape of patient-derived tumor cells informs precision oncology therapy. *Nat. Genet.* **50**, 1399–1411 (2018).
79. MacLeod, G. *et al.* Genome-Wide CRISPR-Cas9 Screens Expose Genetic Vulnerabilities and Mechanisms of Temozolomide Sensitivity in Glioblastoma Stem Cells. *Cell Rep.* **27**, 971–986.e9 (2019).
80. Jacob, F. *et al.* A Patient-Derived Glioblastoma Organoid Model and Biobank Recapitulates Inter- and Intra-tumoral Heterogeneity. *Cell* **180**, 188–204.e22 (2020).
81. Stockslager, M. A. *et al.* Functional drug susceptibility testing using single-cell mass predicts treatment outcome in patient-derived cancer neurosphere models. *Cell Rep.* **37**, 109788 (2021).
82. Shekarian, T. *et al.* Immunotherapy of glioblastoma explants induces interferon-γ responses and spatial immune cell rearrangements in tumor center, but not periphery. *Sci Adv* **8**, eabn9440 (2022).
83. Szklarczyk, D. *et al.* STRING v11: protein-protein association networks with increased coverage, supporting functional discovery in genome-wide experimental datasets. *Nucleic Acids Res.* **47**, D607–D613 (2019).
84. Schaefer, C. F. *et al.* PID: the Pathway Interaction Database. *Nucleic Acids Res.* **37**, D674–9 (2009).
85. Krizhevsky, A., Sutskever, I. & Hinton, G. E. ImageNet classification with deep convolutional neural networks. in *Proceedings of the 25th International Conference on Neural Information*

Processing Systems - Volume 1 1097–1105 (Curran Associates Inc., 2012).

86. Landrum, M. J. *et al.* ClinVar: improving access to variant interpretations and supporting evidence. *Nucleic Acids Res.* **46**, D1062–D1067 (2018).
87. Trapnell, C. *et al.* The dynamics and regulators of cell fate decisions are revealed by pseudotemporal ordering of single cells. *Nat. Biotechnol.* **32**, 381–386 (2014).
88. Miao, Z., Deng, K., Wang, X. & Zhang, X. DEsingle for detecting three types of differential expression in single-cell RNA-seq data. *Bioinformatics* **34**, 3223–3224 (2018).
89. Love, M. I., Huber, W. & Anders, S. Moderated estimation of fold change and dispersion for RNA-seq data with DESeq2. *Genome Biol.* **15**, 550 (2014).
90. Riss, T. L. *et al.* Cell Viability Assays. in *Assay Guidance Manual* (eds. Markossian, S. et al.) (Eli Lilly & Company and the National Center for AdvancingTranslational Sciences, 2013).
91. Kumar, K. S. *et al.* Computer-assisted quantification of motile and invasive capabilities of cancer cells. *Sci. Rep.* **5**, 15338 (2015).
92. Weiss, T. *et al.* NKG2D-Dependent Antitumor Effects of Chemotherapy and Radiotherapy against Glioblastoma. *Clin. Cancer Res.* **24**, 882–895 (2018).